

Probing the existence of very massive first stars

S. Salvadori^{1,2,3*}, P. Bonifacio³, E. Caffau³, S. Korotin⁴, S. Andreevsky^{5,3},
M. Spite³, and Á. Skúladóttir⁶

¹*Dipartimento di Fisica e Astronomia, Università degli Studi di Firenze, Via G. Sansone 1, I-50019 Sesto Fiorentino, Italy*

²*INAF/Osservatorio Astrofisico di Arcetri, Largo E. Fermi 5, I-50125 Firenze, Italy*

³*GEPI, Observatoire de Paris, Université PSL, CNRS, Place Jules Janssen, F-92195 Meudon, France*

⁴*Crimean Astrophysical Observatory, Nauchny 298409, Republic of Crimea*

⁵*Department of Astronomy and Astronomical Observatory, Odessa National University, Isaac Newton Institute of Chile, Odessa Branch, Shevchenko Park, 65014, Odessa, Ukraine*

⁶*Max-Planck-Institut für Astronomie, Königstuhl 17, D-69117 Heidelberg, Germany*

Accepted XXX. Received YYY; in original form ZZZ

ABSTRACT

We present a novel approach aimed at identifying the key chemical elements to search for the (missing) descendants of very massive first stars exploding as Pair Instability Supernovae (PISN). Our simple and general method consists in a parametric study accounting for the unknowns related to early cosmic star-formation and metal-enrichment. Our approach allow us to define the most likely [Fe/H] and abundance ratios of long-lived stars born in inter-stellar media polluted by the nucleosynthetic products of PISN at a > 90%, 70%, and 50% level. In agreement with previous works, we show that the descendants of very massive first stars can be most likely found at [Fe/H] ≈ −2. Further, we demonstrate that to search for an under-abundance of [(N, Cu, Zn)/Fe] < 0 is the key to identify these rare descendants. The “killing elements” N, Zn, and Cu are not produced by PISN, so that their sub-Solar abundance with respect to iron persists in environments polluted by further generations of normal core-collapse supernovae up to a 50% level. We show that the star BD +80° 245, which has [Fe/H] = −2.2, [N/Fe] = −0.79, [Cu/Fe] = −0.75, and [Zn/Fe] = −0.12 can be the smoking gun of the chemical imprint from very massive first stars. To this end we acquired new spectra for BD +80° 245 and re-analysed those available from the literature accounting for Non-Local Thermodynamic Equilibrium corrections for Cu. We discuss how to find more of these missing descendants in ongoing and future surveys to tightly constrain the mass distribution of the first stars.

Key words: galaxies: high-z, dwarf, Local Group; stars: abundances; cosmology: theory.

1 INTRODUCTION

Primordial composition stars were very likely more massive than those that we observe in Local star-forming regions (e.g. Bromm 2013). Analytical calculations (from the pioneering work by Silk (1977) to McKee & Tan (2008)), along with state-of-the-art numerical simulations that include radiative feedback (e.g. Hosokawa et al. 2011), show that the mass of these Population III (Pop III) stars is typically $m_{\text{popIII}} > 10M_{\odot}$, and can reach extreme values when a statistical sample of cosmological formation sites is considered, $m_{\text{popIII}} \approx 1000M_{\odot}$ (Hirano et al. 2014; Susa et al. 2014;

Hirano et al. 2015). On the other hand, 3D simulations following gas fragmentation for $< 10^3$ yrs and resolving individual proto-stars, find that the proto-stellar disk can fragment in sub-solar clumps, which implies the existence of some stars such that $m_{\text{popIII}} < 1M_{\odot}$. On larger time-scales, however, most of these fragments are expected to merge to form more massive stars (e.g. Greif et al. 2012). At the moment, therefore, we can only assert that the characteristic mass of Pop III stars is much larger than normal Pop II/I stars, $m_{\text{popIII}}^{\text{ch}} \approx 10M_{\odot}$, and that their high-mass end possibly extends up to $m_{\text{popIII}} \approx 1000M_{\odot}$ (e.g. Greif 2015; Hirano et al. 2015).

Among such a variety of stellar masses those with $m_{\text{popIII}} > 140M_{\odot}$ represent the dominant sources of ioniz-

* E-mail: stefania.salvadori@unifi.it

ing photons (e.g. [Schaerer 2002](#)), dust (e.g. [Schneider et al. 2004](#)), metals, supernova energy injection, and stellar black holes (e.g. [Heger & Woosley 2002](#)). Pop III stars with $140M_{\odot} < m_{\text{PopIII}} < 260M_{\odot}$ end their lives as energetic Pair Instability Supernovae (PISN), leaving no remnants and thus releasing back to the surrounding gas *all* their mass, with $\approx 50\%$ in the form of heavy elements. Larger Pop III stars, $m_{\text{PopIII}} > 260M_{\odot}$, do not inject metals as they are predicted to directly collapse into stellar black holes (e.g. [Heger & Woosley 2002](#)). Probing the existence and frequency of very massive Pop III stars is thus fundamental to understand the early phases of reionization (e.g. [Salvadori et al. 2014](#)), metal enrichment (e.g. [Pallottini et al. 2014](#)), and super massive black hole formation (e.g. [Volonteri 2010](#)).

One of the most promising ways to test the predicted existence of massive Pop III stars is by identifying their direct descendants among the oldest stars, which can be individually resolved in the Local Group (e.g. [Beers & Christlieb 2005](#); [Tolstoy et al. 2009](#)). If massive Pop III stars rapidly ended their lives as energetic supernovae (SN) explosions, thus preventing their present-day detection, their nucleosynthetic products were efficiently dispersed into the surrounding gas (e.g. [Greif et al. 2009](#); [Smith et al. 2015](#)). Such precious elements from the remote times are safeguarded until the present-day in the photospheres of long-lived low-mass stars, $m_* < 1M_{\odot}$, which form from the ashes of Pop III stars. Different groups have shown that the transition from massive Pop III stars to normal Pop II stars can efficiently take place when the metallicity of the gas clouds reaches a critical value, $Z_{cr} \approx [10^{-6} - 10^{-3.5}]Z_{\odot}$ (e.g. [Bromm et al. 2001](#); [Schneider et al. 2002](#)).

According to cosmological models for the Local Group formation, these “descendants” of Pop III stars can be found among the oldest stellar populations, in particular in the Galactic halo of the Milky Way (e.g. [Tumlinson 2006](#); [Salvadori et al. 2007](#)), in the Galactic bulge ([White & Springel 2000](#); [Brook et al. 2007](#); [Tumlinson 2010](#); [Salvadori et al. 2010](#)), and in nearby dwarf galaxy satellites (e.g. [Salvadori & Ferrara 2009](#); [Bovill & Ricotti 2009](#); [Frebel & Bromm 2012](#); [Salvadori et al. 2015](#)). Local observations have reported the existence of many Carbon enhanced metal-poor (CEMP) stars, $[C/Fe] > 1.0$, in both the Galactic halo (e.g. [Spite et al. 2013](#); [Bonifacio et al. 2015](#), and references therein) and ultra-faint dwarf galaxies (e.g. [Frebel et al. 2014](#); [Spite et al. 2018](#)). These stars predominantly appear at $[Fe/H] < -2.5$. The most iron-poor among them (e.g. [Keller et al. 2014](#)) have chemical abundance patterns that are consistent with the heavy elements produced by moderately massive Pop III stars, $m_{\text{PopIII}} < 100M_{\odot}$, which experience mixing and fallback exploding as “*faint SN*” (e.g. [Bonifacio et al. 2003](#); [Iwamoto et al. 2005](#)), possibly because of their high rotation speed (e.g. [Meynet & Maeder 2002](#)).

The CEMP stars have a bimodal distribution of carbon abundance ([Rossi et al. 2005](#); [Spite et al. 2013](#); [Bonifacio et al. 2015](#)), and the two groups of stars are referred to as “high-carbon band” and “low-carbon band” (see [Bonifacio et al. 2018b](#), for a precise definition). The available evidence points towards the conclusion that the high-carbon band stars are the result of mass-transfer in a binary system, while the low-carbon band stars are a reliable record

of the chemical composition of the interstellar medium from which they were formed (see [Caffau et al. 2018](#), and references therein). We shall adopt this hypothesis in what follows.

The link between low-carbon band CEMP stars and the chemical products of primordial $m_{\text{PopIII}} < 100M_{\odot}$ stars has been confirmed by cosmological chemical evolution models that follow the overall formation of the Local Group (e.g. [Salvadori et al. 2015](#)) or that focus on the build-up of the MW halo (e.g. [de Bressan et al. 2017](#); [Hartwig et al. 2018](#)). These models are able to interpret the declining frequency of low-carbon band CEMP stars at increasing $[Fe/H]$ in a cosmological context (see also [Cooke & Madau 2014](#); [Bonifacio et al. 2015](#)). Their findings show that at $[Fe/H] \leq -5$ roughly 100% of the stars are expected to form in gaseous environments *uniquely* polluted by faint primordial SN with $m_{\text{PopIII}} < 100M_{\odot}$, which produce large amounts of C and small amounts of Fe. At higher $[Fe/H]$, such a key chemical signature is gradually washed-out because of the increasing contribution of normal SN type II to the chemical enrichment (e.g. [Salvadori et al. 2015](#); [de Bressan et al. 2017](#); [Hartwig et al. 2018](#)). This makes the *direct* descendants of moderately massive Pop III stars relatively straightforward to find “just” by searching for the most iron-poor stars.

On the other hand the descendants of very massive PISN are predicted to appear at higher $[Fe/H]$, where they only represent a very low fraction of the total number of stars ([Salvadori et al. 2007](#); [Karlsson et al. 2008](#)). [de Bressan et al. \(2017\)](#) showed that stars which are formed in environments polluted by PISN at $> 50\%$ level cover a broad metallicity range, $-4 < [Fe/H] < -1$, with a peak at $[Fe/H] \approx -1.8$. According to their findings these precious fossils only represent the $\approx 0.25\%$ of the total number of Galactic stars at $[Fe/H] < -2$. Such a percentage becomes even lower, $\approx 0.1\%$, for stars enriched by PISN at $> 80\%$ level. Current observations fully agree with these results. Among the 500 Galactic halo stars analyzed at $[Fe/H] < -2$ *only one*, i.e. $\leq 0.2\%$ of the total, shows a chemical abundance pattern that might be consistent with an environment of formation imprinted *also* by massive PISN ([Aoki et al. 2014](#)). This peculiar star has $[Fe/H] \approx -2.5$, which is the typical iron-abundance of the *direct* descendant of PISN, i.e. stars enriched by PISN at 100% level ([de Bressan et al. 2017](#)). Yet, [Chiaki et al. \(2018\)](#) consider it unlikely that the star observed by [Aoki et al. \(2014\)](#) really is a PISN descendant. In fact, their simulations predict that the direct descendants of PISN are much more rare: only one out of $10^5 - 10^6$ stars.

How can we catch these extremely rare PISN descendants, which are fundamental to characterize the primordial IMF and to understand early galaxy formation processes? In the ongoing era of wide and deep spectroscopic surveys the total number of stars is largely increasing. We can thus face the possibility to find many of these rare stellar relics if we are able to efficiently *identify* them. The aim of this paper is thus to address the following questions:

- What are the key chemical elements we should look for in order to identify the rare descendants of massive Pop III stars, i.e. PISN?
- In gaseous environments enriched both by PISN and normal Pop II stars exploding as core-collapse SN, down to

which fraction of PISN contribution can we still detect its peculiar chemical imprint?

- What are the quantitative prospectives of catching the rare PISN descendants in ongoing and future surveys?

The main problem in addressing these issues is that many of the physical mechanisms regulating the early cosmic star-formation efficiency are largely uncertain. These include the star-formation efficiency of “mini-haloes”, the capability of these systems to retain the metals injected by SN, the metal mixing efficiency, and the typical timescale for metal diffusion and subsequent star-formation. In this paper we present a new, simple, and extremely general parametric study for the chemical evolution of the gas imprinted by the first stellar generations. Our novel approach overcomes the current uncertainties by condensing the unknown physical processes into a few free parameters, which are then varied to explore the full parameter space. Our conclusions are hence general and essentially model independent. Furthermore, they do not rely on the usually assumed (cold) dark matter model.

2 A SIMPLE PARAMETRIC STUDY

We can start by computing the chemical properties of the gaseous environments, or interstellar media (ISM), enriched by the nucleosynthetic products of a *single* Pair Instability SN. The heavy elements yielded by PISN with different initial masses, $m_{\text{PISN}} = [140, 260]M_{\odot}$, have been computed by Heger & Woosley (2002). Because of the peculiar physical conditions that PISN experience during their evolution and the complete disruption of their initial stellar mass, these results are very robust (e.g. Takahashi et al. 2018).

On the other hand, the rate at which the first stars are formed is unknown. State-of-the-art numerical simulations studying Pop III star formation typically focus on low-mass mini-haloes, $M \approx (10^6 - 10^7)M_{\odot}$, which are predicted to be the first star-forming sites at $z > 10$ (e.g. Abel et al. 2002; Wise et al. 2012; Bromm et al. 2009). Molecular hydrogen, H_2 , is the only coolant in these systems, making their capability to form stars limited and variable. The amount of H_2 strongly depends on the total mass, gas density, and formation redshift of the system, along with the presence of Lyman Werner flux from close-by galaxies, which can easily photo-dissociate H_2 (e.g. Madau et al. 2001; Omukai 2012). On top of this variability, cosmological simulations of metal-enrichment show that pristine regions of gas can survive down to $z \leq 3$ (e.g. Pallottini et al. 2014), implying that Pop III stars can also be hosted by more massive galaxies, which have higher star-formation rates.

The ability of the first star-forming systems to convert gas into stars is hence largely uncertain, as it strongly depends on both their intrinsic properties and environmental effects. To make our calculations general we encapsulate these unknowns in a single free parameter, the *star-formation efficiency*, $f_* = M_*/M_g$, which quantifies the mass of Pop III stars, M_* , formed in a dynamical time within a galaxy of initial gas mass M_g . Given the total mass of heavy elements produced per stellar mass formed, i.e. the metal yield Y_Z , we can easily compute the total mass of heavy elements produced by PISN as:

$$M_Z = Y_Z M_* = Y_Z f_* M_g. \quad (1)$$

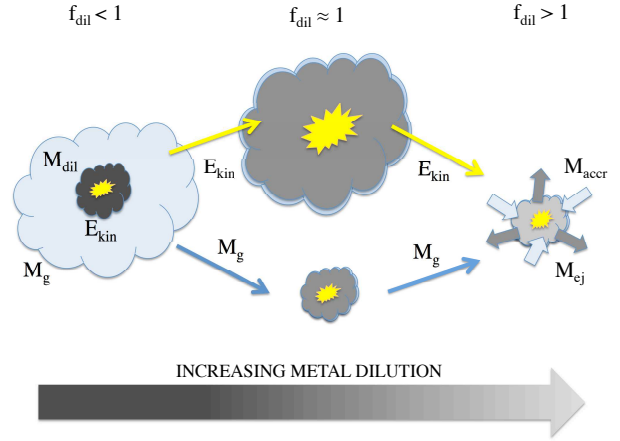


Figure 1. A simple sketch illustrating the mixing of PISN products with the environment for different dilution parameter, f_{dil} , and how it depends on: (i) the kinetic energy released by supernovae, E_{kin} ; (ii) the gas mass of the star-forming galaxy, M_g (cyan cloudlike shape); (iii) the mass into which the PISN products are diluted into, M_{dil} (grey cloudlike shape); (iv) the mass of ejected gas, M_{ej} (grey outgoing arrows); (v) the mass of pristine gas eventually accreted from the IGM, M_{accr} (cyan ingoing arrows). See Sec. 2.1 for details.

Similarly, the net mass of each chemical element X produced by PISN can be computed as $M_X = Y_X f_* M_g$ once the yield Y_X is known. A rough estimate of the metallicity of the ISM after a PISN event can be obtained by assuming that all produced metals are instantaneously mixed within the whole galaxy, i.e. $Z = M_Z/M_g$. In reality, however, not all these fresh metals will necessarily be retained by the galaxy, and/or not all the gas will be used to dilute metals. Indeed, depending upon the kinetic energy released by SN explosions and the mass of the (Pop III) galaxy, metals can fill a different volume of the galaxy, eventually escaping its gravitational potential.

To determine the metallicity of the ISM out of which subsequent star-formation can occur, we should thus quantify: (i) the fraction of newly produced metals effectively retained by the galaxy, $f_Z \equiv (M_Z^{\text{eff}}/M_Z)$; (ii) the fraction of the initial gas mass into which metals are effectively diluted, $f_g = (M_{\text{dil}}/M_g)$. We can encapsulate these two free parameters into a single one, the diluting factor, $f_{\text{dil}} = f_g/f_Z$, which completely defines the ISM metallicity for subsequent star-formation, $Z_{\text{ISM}} \equiv (M_Z^{\text{eff}}/M_{\text{dil}}) = (f_Z M_Z / f_g M_g) = M_Z / f_{\text{dil}} M_g \equiv Z / f_{\text{dil}}$. A qualitative flavour of the possible values of f_{dil} and its dependance upon the unknown metal mixing processes is provided by the sketch in Fig. 1.

2.1 The cosmological context

To understand what are the different physical conditions in which the enriching and mixing events accounted by our simple model might occur, we will discuss Fig. 1 in a cosmological context.

First, if the kinetic energy released by the SN explosions is sufficiently low (e.g. low-mass PISNe) and/or if the star-forming galaxy is massive enough (e.g. mini-halos formed at $z < 10$ or even more massive Ly α -cooling halos), then the

SN blast wave will only fill a small portion of the initial gas mass, $M_{\text{dil}} < M_{\text{g}}$. In such a region, which has been polluted with *all* the newly produced heavy elements (i.e. $f_{\text{Z}} = 1$), the star-formation can be rapidly re-activated thanks to efficient metal-cooling (e.g. Pallottini et al. 2014). We thus have $f_{\text{dil}} < 1$.

Second, if the kinetic energy released by SN explosions is higher than in the previous case (e.g. more massive PISN) and/or if the galaxy is less massive, then the SN blast wave will reach larger radii, possibly mixing all newly produced metals ($f_{\text{Z}} = 1$) within the *whole* galaxy, i.e. $M_{\text{dil}} \approx M_{\text{g}}$. Cosmological simulations have shown that the metal-enriched SN-driven gas confined at the halo virial radius can rapidly cool-down and fall-back into the centre triggering new star-formation (e.g. Oñorbe et al. 2015; Benítez-Llambay et al. 2015). Hence $f_{\text{dil}} \approx 1$.

Third, for even higher SN explosion energy (e.g. high-mass PISNe) and/or less massive galaxies (e.g. the first star-forming mini-halos) the blast wave produced by the explosion can evacuate part (or most) of the metal-enriched gas from the hosting galaxy (e.g. Greif et al. 2007; Chiaki et al. 2018). Both observations and simulations show that the SN-driven outflows are able to eject part of the metals outside of galaxies (e.g. most recently Jones et al. 2018). This implies $f_{\text{Z}} < f_{\text{g}}$ and therefore $f_{\text{dil}} = f_{\text{g}}/f_{\text{Z}} > 1$. In addition, f_{dil} gets even higher if primordial gas accretes onto the galaxy, M_{accr} (e.g. via merging), since f_{Z} remains unchanged while f_{g} increases further. We thus have $f_{\text{dil}} > 1$.

To be more quantitative and appreciate how much different scenarios depend upon the unknown mass of Pop III stars and on the properties of their hosting halos we should recall some recent findings from cosmological simulations. Zoomed-in simulations of the first star-forming mini-haloes at $z > 15$ show that a single energetic PISN explosion ($E_{\text{SN}} \approx 10^{53}$ erg for $m_{\text{PISN}} \approx 260 M_{\odot}$) can evacuate almost all the gas from mini-halos with $M \approx 10^6 M_{\odot}$ (e.g. Greif et al. 2007; Bromm et al. 2003), leading to $f_{\text{dil}} > 1$. Yet, the same mini-halo retains most of the gas/metals after the explosion of the least energetic PISN (e.g. $E_{\text{SN}} \approx 10^{51}$ erg for $m_{\text{PISN}} \approx 150 M_{\odot}$ from Bromm et al. (2003)). In this case, therefore, $f_{\text{dil}} \approx 1$. As we will extensively discuss in Sec. 7, in situ enrichment of mini-halos by PISN can be effectively captures by assuming $f_{\text{dil}} \geq 1$. However, recent cosmological simulations have also shown that a part of the ejected material might pollute a nearby primordial mini-halo, eventually triggering new star-formation there (e.g. Smith et al. 2015, Chiaki et al. 2018). This is equivalent to the case $f_{\text{dil}} < 1$. Although this event it is much more unlikely than the previous two (see e.g. Chiaki et al. 2018), we should also account for this scenario in our general model, which aims at catching the signature of PISNe formed in all the possible physical conditions.

2.2 Chemical imprint

From our previous section we conclude that all the different cosmological scenarios, including both in situ and external pollution along with dilution due to accretion, can be efficiently described by varying our free parameter f_{dil} (Fig. 1). In this context, we are assume that a single PISN forms and explodes and that PISN with different mass have the same probability to form. In fact, a flat primordial IMF

and a single first star per mini-halo is exactly what simulations of the first star-forming systems have found (e.g. Hirano et al. 2014). To account for the (possible) PISN formation in more massive and efficiently star-forming Ly α halos (Sec. 2.1), we extend these hypotheses by assuming that in each star-forming galaxy all formed PISN have the same mass, m_{PISN} . We can thus proceed further and compute the chemical properties of the ISM polluted by a PISN (or more) with mass m_{PISN} . By using the previously defined relations we can compute the ISM metallicity:

$$Z_{\text{ISM}} = M_{\text{Z}}/(f_{\text{dil}}M_{\text{g}}) = \frac{Y_{\text{Z}}^{\text{PISN}}f_{\text{*}}M_{\text{g}}}{f_{\text{dil}}M_{\text{g}}} = \frac{f_{\text{*}}}{f_{\text{dil}}}Y_{\text{Z}}^{\text{PISN}} \quad (2)$$

along with the abundance of any X element into the ISM:

$$\begin{aligned} [X/H]_{\text{ISM}} &\equiv \log\left[\frac{N_{\text{X}}}{N_{\text{H}}}\right] - \log\left[\frac{N_{\text{X}}}{N_{\text{H}}}\right]_{\odot} = \log\left[\frac{M_{\text{X}}}{m_{\text{X}}}\frac{m_{\text{H}}}{M_{\text{H}}}\right] - \log\left[\frac{N_{\text{X}}}{N_{\text{H}}}\right]_{\odot} \\ &\approx \log\left[\frac{M_{\text{X}}}{M_{\text{dil}}}\right] - \log\left[\frac{M_{\text{X}}}{M_{\text{H}}}\right]_{\odot} = \log\left[\frac{f_{\text{*}}}{f_{\text{dil}}}Y_{\text{X}}^{\text{PISN}}\right] - \log\left[\frac{M_{\text{X}}}{M_{\text{H}}}\right]_{\odot}, \quad (3) \end{aligned}$$

where both $Y_{\text{Z}}^{\text{PISN}}$ and $Y_{\text{X}}^{\text{PISN}}$ depend on m_{PISN} , N_{X} (N_{H}) is the number of X (hydrogen) atoms, and m_{X} (m_{H}) the mean molecular weight. Using eq. 3, we can write the abundance ratio of any chemical element with respect to iron (or other key species):

$$[X/Fe]_{\text{ISM}} = \log\left[\frac{Y_{\text{X}}^{\text{PISN}}}{Y_{\text{Fe}}^{\text{PISN}}}\right] - \log\left[\frac{M_{\text{X}}}{M_{\text{Fe}}}\right]_{\odot}. \quad (4)$$

These simple calculations already provide interesting results. The total metallicity of the ISM, Z_{ISM} , along with the $[X/H]$ abundance ratio, *solely* depends on the ratio between the two free parameters of the model, $f_{\text{*}}/f_{\text{dil}}$ and on the total amount of metals (or X elements) produced per stellar mass formed, i.e. the yields. Furthermore, the chemical abundance pattern of the gas uniquely polluted by a PISN (or several PISNe with the same mass) is *solely* determined by the ratios in the chemical yields. In other words it is *universal*. We can thus study the predicted chemical properties of these environments as a function of the PISN mass and $[Fe/H]$ range after defining the most plausible values for the two free parameters, $f_{\text{*}}$ and f_{dil} .

2.3 Setting the free parameter space

The parameter space of the problem, i.e. the possible values of $f_{\text{*}}$ and $f_{\text{*}}/f_{\text{dil}}$, can be estimated analytically. First, local observations of molecular clouds show that the fraction of molecular hydrogen gas (f_{H_2}) that can be turned into stars in a dynamical time never exceed the 10% of the total, i.e. $M_{\text{*}} \times t_{\text{ff}} = \xi_{\text{sf}}f_{\text{H}_2}M_{\text{g}}$ with $\xi_{\text{sf}} \leq 0.1$ (e.g. see Pallottini et al. 2017, and reference therein). Second, the gas needs to be converted in molecular hydrogen form, whose mass fraction is necessarily lower or equal than the total ($f_{\text{H}_2} \leq 1$). By defining $f_{\text{*}} = \xi_{\text{sf}}f_{\text{H}_2}$ we can thus safely set $f_{\text{*}} \leq 0.1$, i.e. we have an upper limit for the star-formation efficiency.

In high-redshift primordial mini-haloes ($T_{\text{vir}} \leq 10^4$ K) which cool-down their gas via molecular hydrogen, $f_{\text{*}}$ is much lower, as it is limited by the fragile nature of H_2 and the lack of additional cooling channels (e.g. Ciardi & Ferrara 2001). Tegmark et al. (1997) showed that only mini-halos

with $f_{\text{H}_2} > 10^{-3}$ can efficiently cool-down their gas and trigger star-formation. Assuming $\xi_{\text{sf}} = 0.1$ we infer $f_* > 10^{-4}$. A similar value is obtained by requiring the formation of at least one PISN per free-fall time in the most massive mini-halos: $f_* \geq M_{\text{PISN}}/M_g = M_{\text{PISN}}/[\Omega_b/\Omega_M M] \approx 2 \times 10^{-4}$, where Ω_b/Ω_M is the cosmological baryon-to-dark matter mass ratio¹ and $M(\text{Tv} \approx 10^4 \text{K}, z = 10) = 5 \times 10^7 M_\odot$ is the mass of the most massive mini-halos, i.e. those with highest T_{vir} and lowest formation redshift (e.g. Barkana & Loeb 2001).

To evaluate the possible f_{dil} values we should distinguish among the different scenarios illustrated in Fig. 1. When $f_{\text{dil}} < 1$ we can estimate the *minimum* gas mass into which all the newly produced metals are diluted as the mass enclosed by the SN-driven bubble in the Sedov-Taylor approximation (e.g. Madau et al. 2001; Bromm et al. 2003):

$$M_{\text{dil}} > \frac{4\pi}{3} \rho_{\text{ISM}} \left(\frac{E_{\text{kin}}}{\rho_{\text{ISM}}} \right)^{3/5} t^{6/5}, \quad (5)$$

where $\rho_{\text{ISM}}(z) \approx 200 \Omega_b \rho_{\text{cr},0} (1+z)^3$ is the ISM gas density, t the time passed since the SN explosions, and

$$E_{\text{kin}} = \langle E_{\text{SN}} \rangle f_{\text{kin}} N_{\text{SN}} = \langle E_{\text{SN}} \rangle f_{\text{kin}} \nu_{\text{SN}} f_* M_g \quad (6)$$

is the kinetic energy released by SN, which depends upon the average SN explosion energy, $\langle E_{\text{SN}} \rangle$, the fraction of energy released in kinetic form which is typically $f_{\text{kin}} \approx 0.1$ (e.g. Pallottini et al. 2014), and the number of SNe, N_{SN} . Since N_{SN} can be written as the number of SN explosion per stellar mass formed, $N_{\text{SN}} = \nu_{\text{SN}} M_* = \nu_{\text{SN}} f_* M_g$, where $\nu_{\text{SN}} \approx 1/200 M_\odot$ for PISN, it is clear from eq. 6 that E_{kin} depends upon the (unknown) star-formation efficiency. Since we want to know the minimum mass of the metal-enriched gas out of which a new star-formation event can eventually occur, we can reasonably evaluate M_{dil} at the free-fall time, $t_{\text{ff}} = (3\pi/32G\rho)^{1/2}$. Recalling that $f_{\text{dil}} = f_g/f_Z$ and that in this case $f_Z = 1$, we can write $f_{\text{dil}} = f_g > M_{\text{dil}}^{\text{min}}/M_g$ and thus:

$$f_{\text{dil}} > 2.4 \times 10^5 \left[\frac{\langle E_{51} \rangle f_{\text{kin}} f_*}{(1+z)} \right]^{3/5} M_g^{-2/5}, \quad (7)$$

where $\langle E_{51} \rangle = \langle E_{\text{SN}} \rangle / 10^{51} \text{erg}$ is the average explosion energy and M_g is expressed in solar masses. From eq. 7 we infer that the minimum f_{dil} corresponds to the largest M_g , highest formation redshift, $z \approx 30$, and minimum $f_* = 10^{-4}$ and $\langle E_{51} \rangle$, which for the least massive PISN is $\langle E_{51} \rangle \approx 1$. By inserting these numbers in eq. 7 and assuming $M_g \approx 10^8 M_\odot$ and $f_{\text{kin}} = 0.1$, we obtain $f_{\text{dil}} > 0.02$. Note that f_{dil} becomes one order of magnitude higher for $\langle E_{51} \rangle \approx 20$, which corresponds to the average PISN mass. Furthermore, as we will see and discuss in Sec. 7.1, M_g , z , and f_* are *not* independent. In particular, the highest z and lowest f_* correspond to the least massive dark matter halos that can trigger star-formation (e.g. Tegmark et al. 1997), from which we get lower M_g and thus higher f_{dil} .

To get the upper limit we should consider the case $f_{\text{dil}} > 1$, and account for the mass of gas/metals ejected outside of the galaxy (M_{ej} and M_{ej}^Z) along with the mass of pristine gas accreted (M^{accr}). We can write $f_g = [M_g(1 - f_* + f_*R) - M_{\text{ej}} + M_{\text{accr}}]/M_g = [1 - f_{\text{ej}} - f_{\text{accr}}]$, where R is the gas fraction returned from stars, which is

¹ We assume cosmological parameters consistent with the Planck 2016 results: $h = 0.65$, $\Omega_b/h^2 = 0.022$, and $\Omega_M = 0.32$

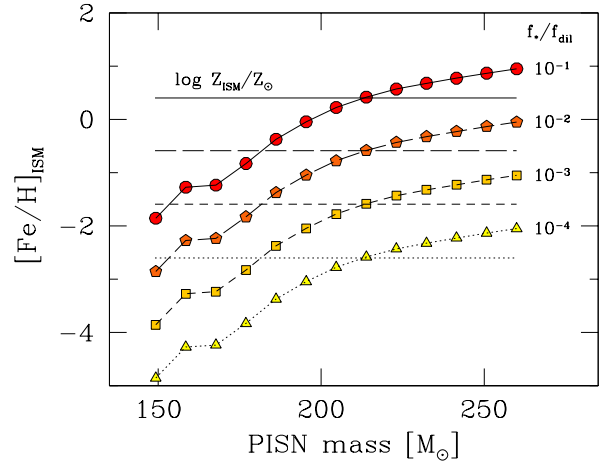


Figure 2. Iron abundance of the ISM imprinted by a PISN as a function of its mass, m_{PISN} (points). Different symbols show the results obtained by assuming various f_*/f_{dil} ratio (see labels). Horizontal lines show the corresponding ISM metallicity, $\log(Z_{\text{ISM}}/Z_\odot)$, which is independent of m_{PISN} .

equal to unity for the case of PISN and f_{ej} (f_{accr}) the fraction of ejected (accreted) gas mass with respect to the total. Assuming that the accreted gas is of primordial composition we can write $f_Z = [M_Z - M_Z^{\text{ej}}]/M_Z = [1 - M_Z^{\text{ej}}/M_Z] = [1 - f_{\text{ej}}\eta_{\text{ej}}]$, where in the last passage we have multiplied and divided for M_g^{ej} and M_g , and defined $\eta_{\text{ej}} = Z_{\text{ej}}/(M_Z/M_g)$. If we assume that the metallicity of the ejected gas is equal to the mean abundance of heavy elements in the galaxy we have $\eta_{\text{ej}} \approx 1$, and thus we can write:

$$f_{\text{dil}} = f_g/f_Z \approx \left(\frac{1 - f_{\text{ej}} + f_{\text{accr}}}{1 - f_{\text{ej}}} \right), \quad (8)$$

from which we infer that the maximum f_{dil} corresponds to the highest f_{accr} and highest f_{ej} . A merging event provides the maximum f_{accr} . To be of primordial composition the merging system should not have experienced previous star-formation, and hence should have a total mass lower than our Pop III star-forming galaxy (e.g. Salvadori & Ferrara 2009). We infer $M_{\text{accr}} \leq M_g$ and thus $f_{\text{accr}} = [0, 1]$. To set the maximum f_{ej} we should recall that we are interested in probing the descendants of very massive first stars. Thus, we need to retain some metals and gas to trigger further star-formation even if $f_{\text{accr}} = 0$. We can fairly assume $f_{\text{ej}} = [0, 0.9]$, from which we obtain $f_{\text{dil}} \leq 10$. As we will discuss in Sec. 7, where we find similar upper limits by developing more detailed calculations, f_{ej} is not independent on f_* . In particular the higher f_{ej} the larger is f_* , which means that the maximum f_{dil} corresponds to the maximum f_* .

In conclusion, we can reasonably state that the dilution factor varies within the range $f_{\text{dil}} \approx (0.02, 10)$ and strongly depends on f_* . Since the lowest (highest) f_{dil} corresponds to the lowest (highest) f_* we obtain $f_*/f_{\text{dil}} \in [10^{-4}, 10^{-1}]$ (see also Sec. 7 and Fig. 21). We can now proceed further since we have established that all the unknowns of the problem are effectively captured by our simple parametrisation.

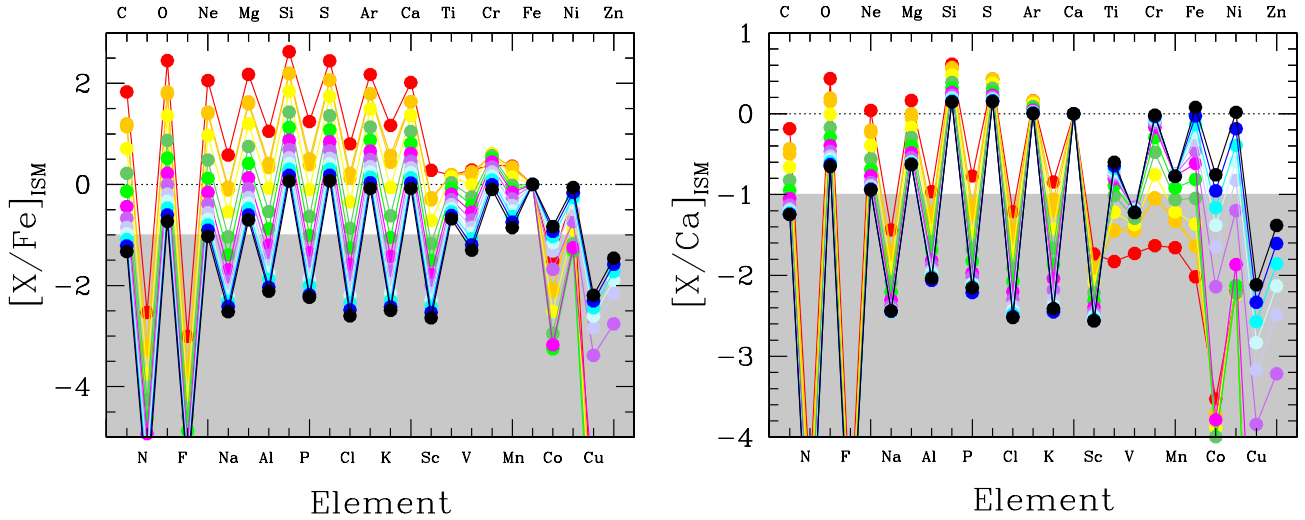


Figure 3. Chemical abundance patterns of the ISM imprinted by a single PISN with increasing mass: from $m_{\text{pop III}} = 150M_{\odot}$ (red) to $m_{\text{pop III}} = 260M_{\odot}$ (black). The injected chemical elements are shown with respect to iron (left) and calcium (right) abundances.

3 RESULTS

In the following we present the results of our simple and general model. We will start by analysing the chemical properties of an ISM solely imprinted by PISN and then extend the calculations to the case in which the chemical products of these massive first stars represent a significant fraction ($\geq 50\%$) of the total mass of heavy elements in the ISM.

3.1 ISM enrichment of a PISN event

The predicted metallicity and iron-abundance values of an ISM imprinted by a single PISN² are shown in Fig. 2, as a function of m_{PISN} , and for different f_*/f_{dil} values (see eq. 1, Sec. 2.1). We see that for any f_*/f_{dil} , the ISM metallicity is larger than any critical metallicity value to trigger the formation of low-mass Pop II stars: $Z_{\text{ISM}} > 10^{-3.5}Z_{\odot}$ (horizontal lines). Thus, long-lived second-generation stars can immediately start to form in a gaseous environment polluted by a single PISN event. These direct descendants of PISN can survive until the present day and hence be observed.

We also notice that $[\text{Fe}/\text{H}]_{\text{ISM}}$ strongly varies with the PISN mass, while Z_{ISM} is basically independent of m_{PISN} . In fact, the lower the iron produced by PISN the higher the oxygen (Heger & Woosley 2002), so that each PISN always injects the same amount of heavy elements into the ISM ($\approx 50\%$ of its mass). Furthermore, at a fixed f_*/f_{dil} , we have that $[\text{Fe}/\text{H}]_{\text{ISM}}$ spans ≤ 1 dex if $m_{\text{PISN}} \geq 200M_{\odot}$, while it might vary by ≥ 2 dex when $m_{\text{PISN}} < 200M_{\odot}$. As a result the “direct descendants of PISN”, i.e. second-generation stars that have been enriched *only* by the chemical product of these massive first stars, span a large $[\text{Fe}/\text{H}]$ range and they are biased towards $[\text{Fe}/\text{H}] > -3$ values. This implies that a very low Fe abundance is *never* a good tracer of these rare stars. What about the other chemical elements?

In Fig. 3 we show the predicted chemical abundance

pattern of an ISM polluted by PISN with different masses normalized to iron, $[\text{X}/\text{Fe}]_{\text{ISM}}$, and calcium, $[\text{X}/\text{Ca}]_{\text{ISM}}$. We recall that these abundance ratios are independent on the assumed free parameters (eq. 4). By focusing on the chemical imprint of a *single* PISN (each color) we can see the so-called “odd-even” effect, which has been historically looked for in ancient metal-poor stars but which has never been unambiguously observed. By inspecting the results for different m_{PISN} more closely, we note that $[\text{X}/\text{Fe}]_{\text{ISM}}$ can vary by more than 2 orders of magnitudes for each chemical species. This implies that it is extremely difficult to identify a “typical” abundance pattern of an ISM imprinted by a population of PISN, i.e. by more than one PISN with different mass. Yet, we can see that there are some key elements, i.e. N, F, Cu, and Zn, which are systematically under-produced with respect to iron, i.e. $[\text{X}/\text{Fe}]_{\text{ISM}} < -1$. Searching for the lack of such key chemical species in large stellar surveys can be an effective way to pre-select PISN candidates for high-resolution follow-up.

We should note here that in large stellar surveys often $[\text{Fe}/\text{H}]$ is inferred either from the CaII K line only (e.g. Starkenburg et al. 2017), or this line has a very high weight in the determination of $[\text{Fe}/\text{H}]$ (e.g. Aguado et al. 2017; Allende Prieto et al. 2014). In other words Ca is implicitly assumed to be a good tracer of Fe and the well known evolution of $[\text{Ca}/\text{Fe}]$ in the Milky Way, is folded into the analysis method (e.g. Bonifacio et al. 2011). Our results, however, show that this is not the case for an ISM uniquely imprinted by PISN, as $[\text{Ca}/\text{Fe}]$ spans more than two orders of magnitudes depending on m_{PISN} . In Fig. 3b we show the predicted chemical abundance pattern of an ISM polluted by a single PISN normalized to Ca. We see that several elements are under-produced with respect to Ca: N, F, Na, Sc, V, Cu, and Zn. Among them, we can identify our *four key elements*, which can then be used to guide observational searches of gas/stars imprinted by PISN.

² Or by several PISNe with the same mass, m_{PISN} .

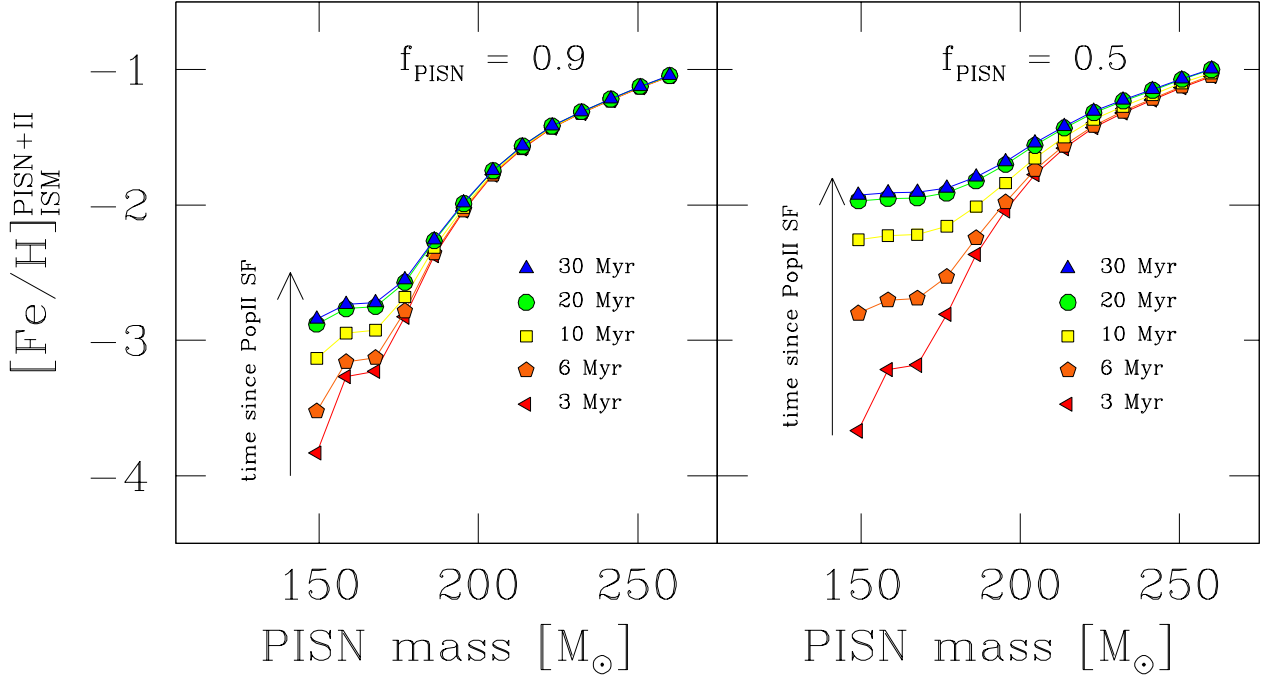


Figure 4. Iron abundances of an ISM imprinted by both PISN of mass m_{PISN} and the subsequent generation of Pop II stars. The results refer to the model $f_*/f_{\text{dil}} = 10^{-3}$ (Fig. 2 and text), and assume $f_{\text{PISN}} = 0.9$ (left) and $f_{\text{PISN}} = 0.5$ (right). Different symbols show the expected values at different times since the onset of Pop II star-formation (see labels).

3.2 Subsequent Pop II star-formation

In our previous Section we showed that an ISM imprinted by PISN at a 100% level, i.e. the birth environment of the direct descendants of very massive first stars, shows a deficiency of N, F, Cu, and Zn. We can thus use these key chemical elements to identify their missing descendants. However, we know that second-generation stars only imprinted by PISN are extremely rare (e.g. Salvadori et al. 2007; de Bannassuti et al. 2017; Chiaki et al. 2018). We can thus try to extend our search to stars imprinted by both PISN and a subsequent generation of Pop II stars. We then face two questions. How does the chemical abundance pattern of an ISM pre-enriched by PISN evolve when we account for the contribution of “normal” Pop II stars? Is the deficiency of the four key chemical elements preserved?

To address these questions we can re-write the equations presented in Sec. 2 as a function of the mass of heavy elements contributed by PISN, $M_Z^{\text{eff}} = f_Z M_Z$, with respect to the total mass of metals effectively injected into the ISM, i.e. $f_{\text{PISN}} = (f_Z M_Z)/M_Z^{\text{tot}}$, where $M_Z^{\text{tot}} = f_Z M_Z + M_Z^{\text{II}}$ is the total mass of metals into the ISM and M_Z^{II} is the mass dispersed by Pop II stars. To ensure that PISN dominate the metal enrichment we will vary this new free parameter in the range $f_{\text{PISN}} = [0.5, 1.0]$. Analogously to what we have done in eq. 1, we can write $M_Z^{\text{II}} = M_*^{\text{II}} Y_Z^{\text{II}}(m_{\text{II}}(t, Z_*))$ from which we get:

$$M_Z^{\text{II}} = Y_Z^{\text{II}}(t, Z_*) f_*^{\text{II}} M_g^{\text{II}} \equiv Y_Z^{\text{II}}(t, Z_*) f_g^{\text{II}} M_g, \quad (9)$$

where Y_Z^{II} is the metal yields of Pop II stars and f_*^{II} is the efficiency at which Pop II stars formed in the PISN-polluted ISM, with a gas mass $M_g^{\text{II}} \equiv f_g M_g$ (see Sec. 2.1 for details). Note that the yields of Pop II stars depend on both the

stellar metallicity (i.e. $Z_* = Z_{\text{ISM}}$, eq. 2, Fig. 2) and the time passed since the Pop II star formation, t_{popII} , which sets the mass of Pop II stars contributing to the metal enrichment, m_{popII} . Given the broad mass range of Pop II stars that can explode as core-collapse supernovae (SNII), $m_{\text{popII}} = (8 - 40)M_{\odot}$, such timescale can vary from a few Myr to tens of Myr, as is shown in Fig. 5.

To ensure the generality of our results we study the problem at various times, i.e. for each f_{PISN} we investigate how the ISM abundance pattern varies when SNII of different masses contribute to the chemical enrichment. Before doing so we determine the star-formation rate of Pop II stars in the ISM pre-enriched by PISN. By using the relation $M_Z^{\text{II}} = M_Z^{\text{tot}} - f_Z M_Z = M_Z \times [(1 - f_{\text{PISN}})/f_{\text{PISN}}]$ we get:

$$f_*^{\text{II}} = \frac{f_*}{f_{\text{dil}}} \frac{Y_Z^{\text{PISN}}}{Y_Z^{\text{II}}} \frac{1 - f_{\text{PISN}}}{f_{\text{PISN}}} = \frac{f_*}{f_{\text{dil}}} \frac{Y_Z^{\text{PISN}}}{Y_Z^{\text{II}}} \beta, \quad (10)$$

where for simplicity we have omitted the yield dependence on Z_* , t_{popII} (or m_{popII}), and m_{PISN} , and so we will do hereafter. The relative amount of metals contributed by Pop II with respect to PISN is $\beta = \left(\frac{1 - f_{\text{PISN}}}{f_{\text{PISN}}}\right)$, where $f_{\text{PISN}} \in [0.5, 1.0]$. Hence, eq. 10 is telling us that for any f_*/f_{dil} model, f_*^{II} is fully determined by the PISN-to-Pop II metal yield ratio, $Y_Z^{\text{PISN}}/Y_Z^{\text{II}}$, once β has been fixed. Note that, analogously to what we discussed for f_* , the PopII star-formation efficiency should be $f_*^{\text{II}} \leq 0.1$ (Sec. 2).

The metallicity of an ISM polluted by both a PISN and a subsequent generation of normal SNII is then: $Z_{\text{ISM}}^{\text{PISN+II}} = (f_Z^{\text{II}} M_Z^{\text{tot}})/(M_g f_{\text{dil}} f_g^{\text{II}}) = M_Z^{\text{tot}}/(M_g f_{\text{dil}} f_g^{\text{II}})$, where $f_{\text{dil}}^{\text{II}}$ accounts for the dilution of metals into the ISM. Similarly to what we saw for f_{dil} (see Sec. 2 for details), $f_{\text{dil}}^{\text{II}}$ resides in

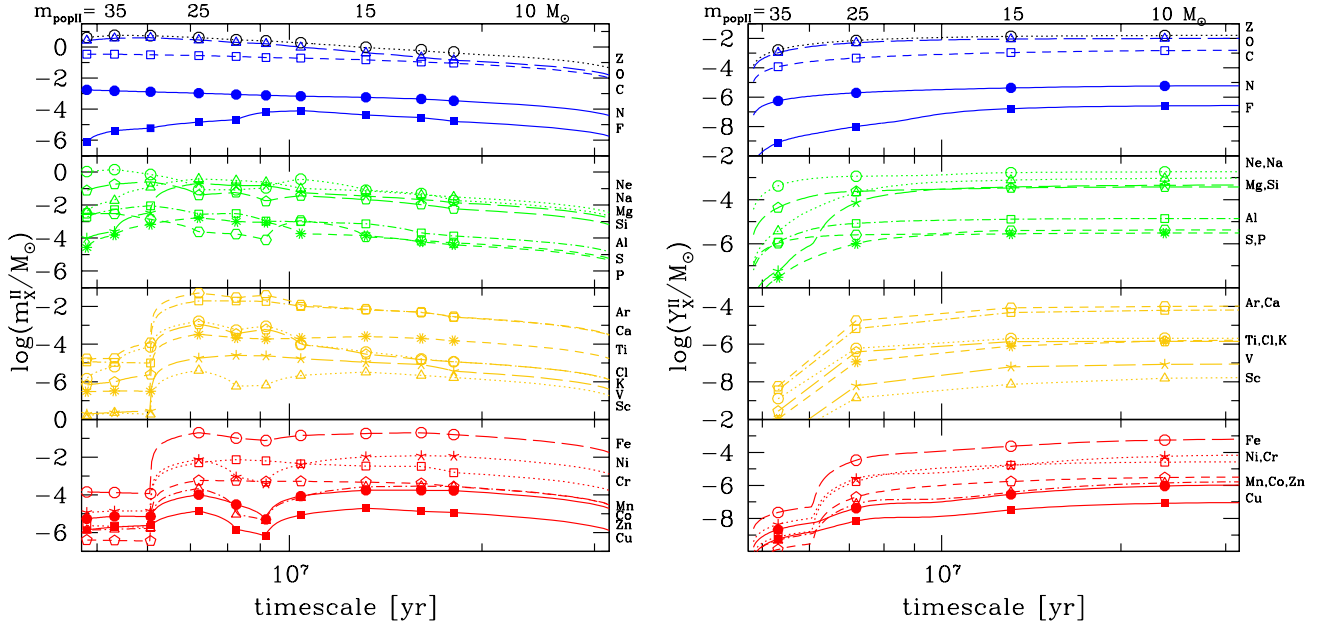


Figure 5. Chemical products of Pop II stars with $Z_* = 0.01Z_\odot$, i.e. typical of an environment enriched by a single PISN. Symbols/lines refer to different chemical species (see labels). *Left:* Mass of chemical elements produced by individual Pop II stars with various m_{popII} , which therefore evolve with different (life)times. *Right:* Yields of Pop II stars, i.e. cumulative mass of chemical elements produced per stellar mass formed, as a function of time since the Pop II formation. In both panels the points show the values obtained by using the data from Woosley & Weaver (1995). The lines are the interpolated values over the SNIID mass range

a relatively tight range, which is even narrower in the case of Pop II stars since $\langle E_{51} \rangle \approx 1$ independent of the SNIID mass. Therefore we approximate $f_{\text{dil}}^{\text{II}} \approx 1$ and get the equivalent of eq. 2:

$$Z_{\text{ISM}}^{\text{PISN+II}} = \frac{Y_Z^{\text{PISN}}}{f_{\text{PISN}}} \frac{f_*}{f_{\text{dil}}} \quad (11)$$

and of eq. 3:

$$[\text{X}/\text{H}]_{\text{ISM}}^{\text{PISN+II}} = \log \left[\frac{f_*}{f_{\text{dil}}} \left[Y_X^{\text{PISN}} + \beta \frac{Y_X^{\text{II}} Y_Z^{\text{PISN}}}{Y_Z^{\text{II}}} \right] \right] - \log \left[\frac{M_X}{M_{\text{Fe}}} \right]_{\odot} \quad (12)$$

which are functions of the free parameters f_*/f_{dil} , f_{PISN} , m_{PISN} , and of the time passed since the formation of Pop II stars, t_{popII} . Thus, for each m_{PISN} and f_*/f_{dil} value (see Fig. 2), we can compute how Z_{ISM} and $[\text{Fe}/\text{H}]_{\text{ISM}}$ evolve for different f_{PISN} .

The results of our calculations are displayed in Fig. 4. By construction the SNIID contribution only alters the total ISM metallicity by a factor $(1 - f_{\text{PISN}}) \leq 0.5$. On the other hand, it has a large impact on the iron abundance. This effect is particularly relevant for an ISM enriched by PISN with $m_{\text{PISN}} < 200M_\odot$, which only convert $< 0.001\%$ of their mass in iron. Furthermore, it is more pronounced when the PISN contribution to the ISM enrichment is lower, $f_{\text{PISN}} = 0.5$. In conclusion, *the subsequent contribution of normal Pop II stars pushes towards more similar, and thus higher, $[\text{Fe}/\text{H}]_{\text{ISM}}$ values.*

These results can be better understood by inspecting Fig. 5 (left), which shows the mass of each chemical species,

m_X^{II} , yielded by Pop II stars with various masses as predicted by the models of Woosley & Weaver (1995). These quantities depends both on the mass of Pop II stars, which evolve on different timescales, and on their metallicity. As example, we only show the case $Z_* = Z_{\text{ISM}} = 0.01Z_\odot$, which is a typical ISM metallicity after a PISN event (Fig. 2). It is clear from the Figure that that while most of the metals (mainly oxygen) are provided by massive Pop II stars, $m_{\text{popII}} > 20M_\odot$, the iron produced by SNIID is predominantly yielded by $m_{\text{popII}} < 20M_\odot$ stars, i.e. on longer time-scales.

In the right panel of Fig. 5, we show the time dependent SNIID yields, Y_X^{II} , i.e the cumulative mass of heavy elements injected by Pop II stars as a function of time since their formation epoch. Once Z_* has been fixed the time-dependent yields are obtained as: $Y_X^{\text{II}}(t) = \int_{m_{\text{popII}}(t)}^{100M_\odot} m_X^{\text{II}} \Phi(m_*) dm_*$, where we have used the time and metallicity-dependent stellar lifetimes by Raiteri et al. (1996), and a standard Larson IMF³ (e.g. Salvadori et al. 2008). We see that the longer the time since the Pop II star-formation, the higher the number of SNIID contributing to the ISM enrichment, and so the larger Y_X^{II} . Yet, while Y_Z^{II} reaches approximately the final value at $t_{\text{popII}} \approx 10$ Myr, at the same t_{popII} we have that $Y_{\text{Fe}}^{\text{II}}$ is only $< 10\%$ of the total iron mass produced after $t_{\text{popII}} \approx 20$ Myrs.

By using Y_X^{II} and eq. 12, we can finally compute the chemical abundance pattern of an ISM enriched by a PISN

³ We adopt a Larson IMF: $\Phi(m_*) = A(m_*/0.35M_\odot)^{-2.35}$ with $m_* = (0.1, 100)M_\odot$, and normalization constant A.

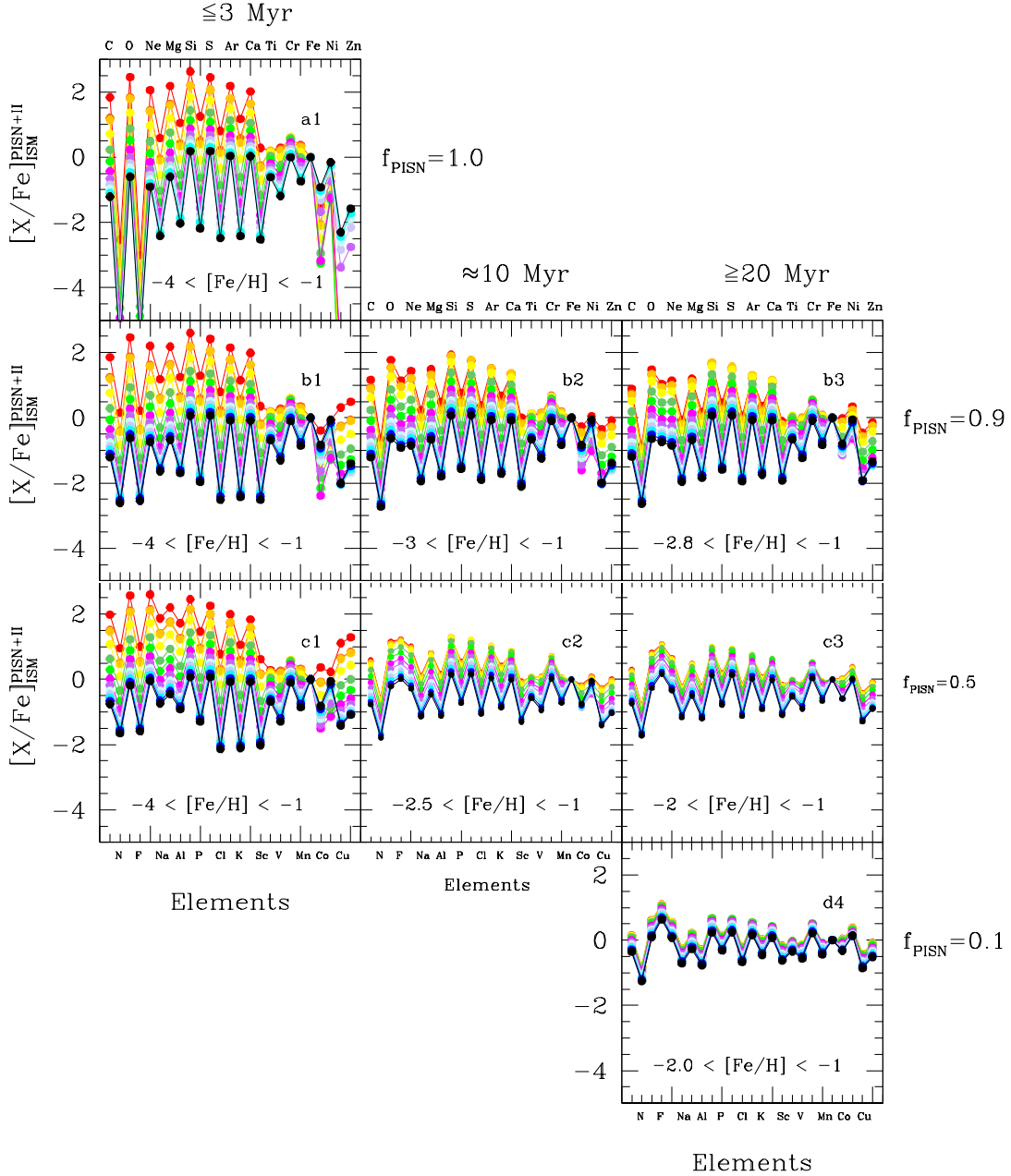


Figure 6. Possible chemical abundance patterns of an ISM imprinted by PISN with different masses (colors as in Fig. 3) and a subsequent generation of normal Pop II stars exploding as core-collapse SN. Different rows show how the results change by varying the total amount of metals in the ISM contributed by PISN: 90% (panels b), 50% (panels c). For comparison we also show two extreme cases: 100% contribution from PISN (panel a1), and 10% contribution from PISN, which implies that 90% of the heavy elements are provided by Pop II stars in a ≈ 20 Myr time-scale (panel d4). Different columns refer to different times since the Pop II formation: $t_{\text{popII}} \approx (3, 10, 20)$ Myr (panels 1, 2, and 3). In each panel the corresponding $[\text{Fe}/\text{H}]$ range for the f_{PISN} and t_{popII} values is reported in the labels. The results refer to the case $f_*/f_{\text{dil}} = 10^{-3}$.

and subsequent SNI:

$$[\text{X}/\text{Fe}]_{\text{ISM}}^{\text{PISN+II}} = \log \left[\frac{Y_{\text{X}}^{\text{PISN}} + \beta \frac{Y_{\text{Z}}^{\text{PISN}}}{Y_{\text{Z}}^{\text{II}}} Y_{\text{X}}^{\text{II}}}{Y_{\text{Fe}}^{\text{PISN}} + \beta \frac{Y_{\text{Z}}^{\text{PISN}}}{Y_{\text{Z}}^{\text{II}}} Y_{\text{Fe}}^{\text{II}}} \right] - \log \left[\frac{M_{\text{X}}}{M_{\text{Fe}}} \right]_{\odot}. \quad (13)$$

Equations 11, 12, and 13 respectively give back eq. 2, eq. 3, and eq. 4 when $\beta \rightarrow 0$ or $f_{\text{PISN}} = 1$, i.e. when the overall

amount of metals into the ISM is provided by PISN. Similar to the case of PISN (eq. 4), we see that eq. 13 does not depend on f_*/f_{dil} . Note however that f_*/f_{dil} , together with m_{PISN} , sets the stellar metallicity, $Z_* = Z_{\text{ISM}}$, thus influencing the chemical yields (Sec. 4). We therefore conclude that $[\text{X}/\text{Fe}]_{\text{ISM}}^{\text{PISN+II}}$ depends on all the free parameters of our model: (i) the PISN mass, m_{PISN} , which sets $Y_{\text{X}}^{\text{PISN}}$ and to-

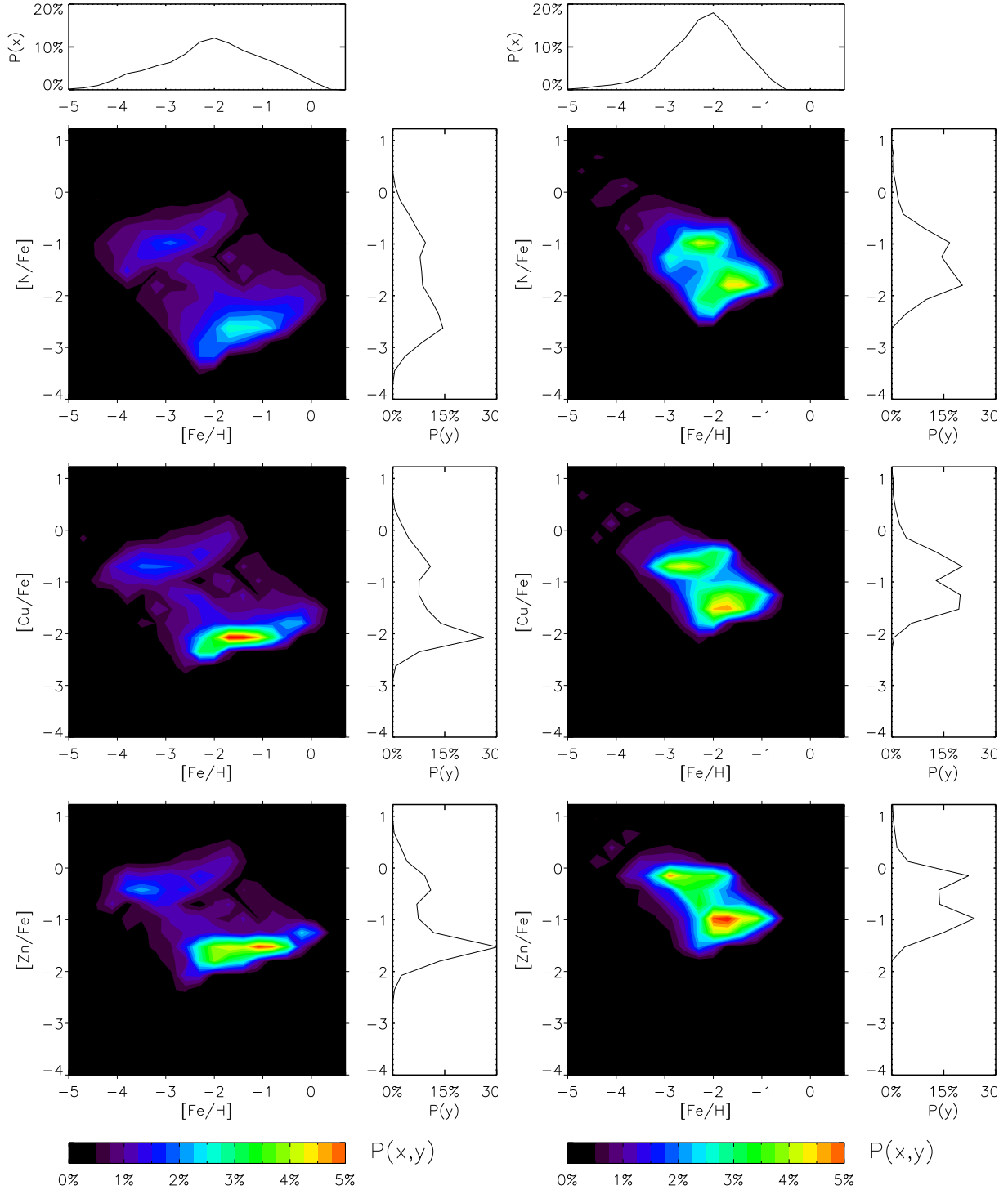


Figure 7. For the three key elements N (*upper panels*), Cu (*middle*), and Zn (*lower*), we show the most likely $[\text{X}/\text{Fe}]$ vs $[\text{Fe}/\text{H}]$ values for an ISM imprinted by PISN at a 90% (*left*) and 50% (*right*) level, i.e. for $f_{\text{PISN}} = 0.9$ and $f_{\text{PISN}} = 0.5$. The histograms on the top (right) show the corresponding probability functions for $[\text{Fe}/\text{H}]$ ($[\text{X}/\text{Fe}]$).

gether with f_*/f_{dil} determines $Z_{\text{ISM}} = Z_*$; (ii) the time t_{popII} passed since the Pop II formation, which sets $Y_{\text{X}}^{\text{II}}(t, Z_*)$; and (iii) the total fraction of metals contributed by PISN, f_{PISN} . Hence, by exploring the overall parameter space we can fully investigate how the chemical abundance patterns of an ISM imprinted by PISNe varies after the formation of subsequent

Pop II stars, and under which conditions the deficiency of the key chemical species discussed in Sec. 3.1 is preserved.

The results of eq. 13 are shown in Fig. 6 for $f_*/f_{\text{dil}} = 10^{-3}$. We see that the peculiar chemical signatures of PISNe, i.e. the so-called odd-even effect (panel a), is mostly preserved when the contribution of Pop II stars to the chemi-

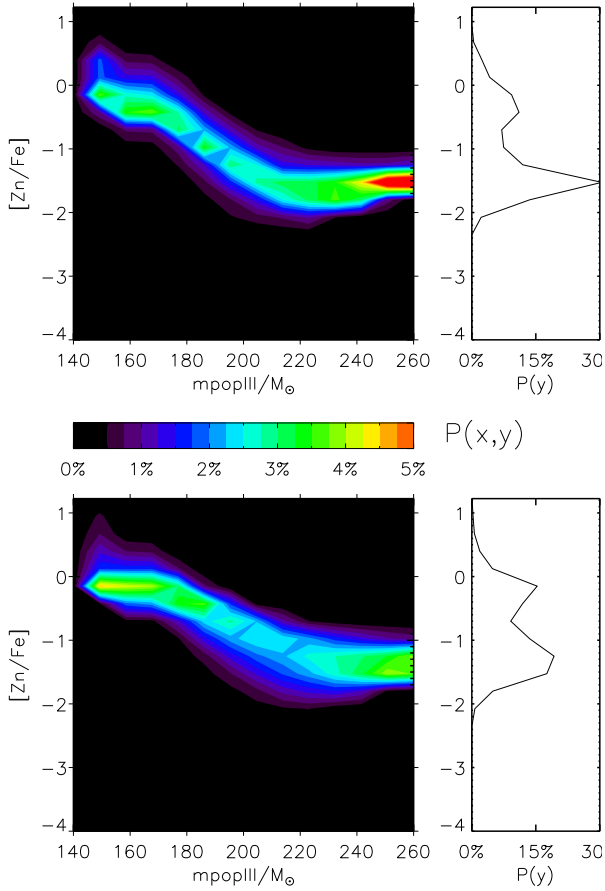


Figure 8. Most likely $[Zn/Fe]$ vs m_{PISN} values for an ISM imprinted by PISN at a 90% (*top*) and 50% (*bottom*) level. As in Fig. 7 the histograms on the right show the corresponding probability distribution functions for $[Zn/Fe]$.

cal enrichment is $\approx 10\%$ of the total (panels b). Yet, the effect is less prominent than before since those elements that were completely lacking in ejecta of PISN (e.g. N, F) are largely produced by massive SNII, yielding a finite, although low, $[X/Fe]$ abundance ratios (panels b vs panel a). Furthermore, while the time passes and less massive Pop II stars begin to contribute to the ISM enrichment, the over-abundance of even elements becomes less and less pronounced because of the larger amount of iron produced, which reduces the $[X/Fe]$ ratios (panels b2-b3). Finally, both the odd-even chemical signatures and the large variation of $[X/Fe]$ for different m_{PISN} get gradually lost when the total amount of metals from low-mass SNII, $m_{\text{popII}} \leq 20$, equals those from PISN (panels c2-c3). When $f_{\text{PISN}} = 0.1$, they are almost completely washed-out (panel d). With the only exception of F, which is largely produced by Pop II stars yielding $[F/Fe] > 0$ in most cases, we can see in Fig. 6 that when $f_{\text{PISN}} \geq 0.5$ the majority of our models provide $[(N, Cu, Zn)/Fe] < -1$. Hence, we can effectively use the deficiency of these three key species to trace ISM/stars imprinted by very massive PISN at $> 50\%$ level.

4 PISN DESCENDANTS: KEY ELEMENTS

With the only exception of F, which is largely produced by normal Pop II stars, the lack of N, Cu, and Zn with respect to Fe is preserved in environments enriched by PISN at $> 50\%$ level. To be able to use these key elements as tracers of PISN enrichment, we should then address the following questions: (1) How much do our results depend upon f_*/f_{dil} ? (2) What are the typical $[Fe/H]$ values of ISM and stars imprinted by PISN?

Fig. 7 shows the most likely $[(N, Cu, Zn)/Fe]$ vs $[Fe/H]$ ISM abundance ratios for $f_{\text{PISN}} = (0.9, 0.5)$ and all the possible f_*/f_{dil} , m_{PISN} , and t_{popII} values. The histograms reported in upper/right panels are obtained by respectively integrating the probability maps over $[X/Fe]$ and $[Fe/H]$. Independent of the relative contribution of PISN to the ISM enrichment, i.e. for different f_{PISN} , we see that the $[Fe/H]$ covers a large range of values the most common being $[Fe/H] \approx -1.8$. These histograms represent the metallicity distribution function (MDF) of stars imprinted by PISN at $> 90\%$ and $> 50\%$ level. The peak of these MDFs nicely coincides with the one found by de Bressan et al. (2017). However, our calculations are simpler and more generic, since they do not depend on the assumed (cold) dark matter model, nor on the specific environment of PISN formation (e.g. mini-halos).

For all the key elements in Fig. 7 the probability distribution functions of the most likely $[X/Fe]$ abundance ratios exhibit two peaks, one at $[X/Fe]_{\text{low}} < -1$, and the other at higher values, $[X/Fe]_{\text{high}}$. When $f_{\text{PISN}} = 0.9$, $[X/Fe]_{\text{low}}$ is more pronounced than the other one and we see that $P([X/Fe]_{\text{low}}) \approx 2 \times P([X/Fe]_{\text{high}})$ for both Cu and Zn. On the other hand, when $f_{\text{PISN}} = 0.5$ the two peaks are of similar size. Moreover, while $[X/Fe]_{\text{high}}$ almost coincides with what we found for $f_{\text{PISN}} = 0.9$, we see that $[X/Fe]_{\text{low}}$ is shifted towards higher abundance ratios by ≈ 0.5 dex.

In Fig. 8 we demonstrate the origin of these peaks by showing the case of $[Zn/Fe]$. We immediately see that $[X/Fe]_{\text{high}}$ is produced by the chemical enrichment of low-mass PISN, $m_{\text{PISN}} \leq 180 M_{\odot}$, while $[X/Fe]_{\text{low}}$ is caused by more massive PISN. To understand why one peak is more pronounced than the other when $f_{\text{PISN}} = 0.9$ we should inspect the b-panels of Fig. 6. By comparing the panels b1, b2, and b3, which respectively refer to $t_{\text{popII}} = (3, 10, 30)$ Myr, we see that the $[Zn/Fe]$ ratios of the $m_{\text{PISN}} \leq 180 M_{\odot}$ models (yellow, orange, and red symbols) vary by more than 1 dex. Conversely, models with $m_{\text{PISN}} > 180 M_{\odot}$ (from green to black symbols), show very similar $[Zn/Fe]$ values across the whole t_{popII} range, which is mainly due to the constant $[Fe/H]$ values they produce (Fig. 4, left). As a result of these features we have that $P([X/Fe]_{\text{high}}) \approx 2P([X/Fe]_{\text{low}})$ for $f_{\text{PISN}} = 0.9$. In the right panel of Fig. 4, we see that when $f_{\text{PISN}} = 0.5$ models with $m_{\text{PISN}} > 180 M_{\odot}$ provide different $[Fe/H]$ for various t_{popII} . As a result their $[Zn/Fe]$ distributions are less peaked than in the previous case (Fig. 8). On the other hand, in Fig. 4 (right) we see that models with $m_{\text{PISN}} \leq 180 M_{\odot}$ show exactly the same $[Fe/H]$ when $t_{\text{popII}} \geq 20$ Myr, which results in a higher $P([X/Fe]_{\text{high}})$. The combination of these effects for $f_{\text{PISN}} = 0.5$ causes $P([X/Fe]_{\text{high}}) \approx P([X/Fe]_{\text{low}})$.

In Fig. 9 we show the results for the most likely $[Zn/Fe]$ and $[Cu/Fe]$ of an ISM enriched by PISN at a 90% and 50% level. When the highly varying $[Fe/H]$ is not included (e.g.

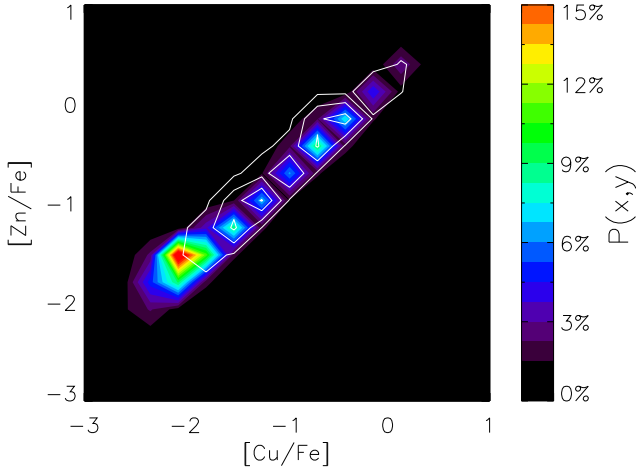


Figure 9. Most likely $[Zn/Fe]$ vs $[Cu/Fe]$ values for an ISM imprinted by PISN at a 90%, (coloured contours and bar for the corresponding probability) and 50% level (over-plotted white contours corresponding to probabilities $P = (1, 5, 10, 15)\%$).

Fig. 4 for its dependance on f_{PISN} , m_{PISN} , and t_{popII} , the most probable abundance space is greatly reduced. Furthermore it essentially lies in a line since Zn and Cu are both Fe-peak elements, which are mainly produced during the explosive phase of SN.

In conclusion, by identifying ISM gas or stars with $[N/Fe] < -1.5$, $[Cu/Fe] < -1$, $[Zn/Fe] < -0.5$, and that reside in the broad range $-3 < [Fe/H] < -1$, we should maximize the probability to find gas/stars imprinted by PISN at $\geq 50\%$ level. Before comparing our results with available data from the literature to look for interesting candidates, we should discuss the robustness of these findings. To this end we will examine in detail the SNII time-dependent yields exploited in our calculations and we will analyze the possible effects on the ISM enrichment of supernovae Ia (SNIa), which represent important sources of metals at $[Fe/H] > -2$.

4.1 A deeper look at the SNII yields

We have shown that the deficiency of the three key elements N, Cu, and Zn with respect to Fe is a good tracer of a chemical imprint from PISN. Indeed, such elements are so scarcely produced by PISN (Fig 3) that even when the ISM is polluted by subsequent SNII at $\geq 50\%$ level their under-production with respect to Fe persist. We can then ask: are we sure not to underestimate $[(N,Cu,Zn)/Fe]$ yields from SNII?

In Fig. 10 we show the $[(N,Cu,Zn)/Fe]$ yields for Pop II stars with different masses (lifetimes) and metallicities as derived by various authors (left vs middle) and by using different models. In the left-most panel of Fig. 10 we report the Woosley & Weaver (1995) outputs for the three models published in their paper (A, B, and C) for core-collapse SN with masses $m_{\text{popII}} = (30, 35, 40)M_{\odot}$. These models differ for the SN explosion energy, the A model being the standard case ($E_{SN} \approx 10^{51}$ erg). For all these models we halved the iron yields as suggested by Timmes et al. (1995).

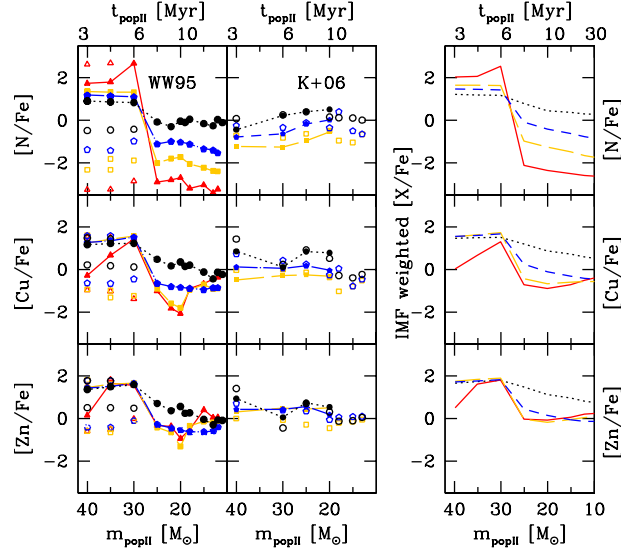


Figure 10. Abundance ratio from Pop II stars with different masses/lifetimes and metallicities. Lines show the linearly interpolated values among different masses. *Left:* $[X/Fe]$ values from Woosley & Weaver (1995) for metallicities $Z_* = 10^{-4}Z_{\odot}$ (red triangles, solid lines), $Z_* = 0.01Z_{\odot}$ (yellow squares, long-dashed), $Z_* = 0.1Z_{\odot}$ (blue pentagons, short-dashed), and $Z_* = Z_{\odot}$ (black circles, dotted). Model A assumed in our calculations is shown with filled symbols. Open symbols show models B and C (see text). *Middle:* $[X/Fe]$ values for core-collapse SN (open symbols) and hypernovae (filled symbols) from Kobayashi et al. (2006) for metallicities $Z_* = 0.05Z_{\odot}$ (yellow squares, long-dashed), $Z_* = 0.2Z_{\odot}$ (blue pentagons, short-dashed), and $Z_* = Z_{\odot}$ (black circles, dotted). *Right:* IMF weighted $[X/Fe]$ yields used in our calculations and derived using model A of Woosley & Weaver (1995) (see left panel, same colors/symbols).

This automatically produces higher $[X/Fe]$ ratios, so we are not underestimating them. From Fig. 10 we can see that the standard model (A), which is assumed in our calculations, gives the largest $[X/Fe]$ abundance ratios in almost all cases. Furthermore, we note that massive core-collapse SN with $m_{\text{popII}} \geq 30M_{\odot}$ provide the highest contribution to $[(N,Cu,Zn)/Fe]$ abundance ratios, and that such values are even higher than those provided by Kobayashi et al. (2006) (right panel), which include the effects of both normal core-collapse SN and more energetic “hypenovae”.

Massive $m_{\text{popII}} \geq 30M_{\odot}$ stars have the shortest lifetimes, $t_{\text{popII}} < 6$ Myr, and hence they can promptly start contributing to the chemical enrichment by injecting large amounts of $[(N,Cu,Zn)/Fe]$. Our calculations account in two ways for these high $[(N,Cu,Zn)/Fe]$ producers. In fact, to evaluate the possible abundance patterns of ISM/stars polluted by both PISN and Pop II stars we use IMF integrated yields over times (masses) since the Pop II formation (Fig. 10, right). So, on one hand, while evaluating the results at $t_{\text{popII}} < 6$ Myr we consider the possibility to have an ISM *only* imprinted by PISN and *massive* core-collapse SN. On the other hand, while computing the results at later times, we *always* account for the contribution of $m_{\text{popII}} \geq 30M_{\odot}$ core-collapse SN that exploded before. Note that in low-mass inefficiently star-forming systems (e.g. mini-halos), massive stars might form at a much lower rate than pre-

dicted by the theoretical IMF because of its poor sampling (e.g. de Bressan et al. 2017). Hence massive Pop II stars, i.e. the higher $[(N,Cu,Zn)/Fe]$ producers, might form at a lower rate. Ultimately, we can surely assert that the lack of $[(N,Cu,Zn)/Fe]$ in ISM/stars imprinted by PISN and Pop II stars is not an artefact of our assumptions.

4.2 Is there a degeneracy with the SNIa imprint?

Recent measurements of zinc and iron abundances for individual red giant branch stars in the Milky Way (Duffau et al. 2017; Barbuy et al. 2015) and in nearby dwarf galaxies (Skúladóttir et al. 2017, 2018) have reported low zinc over iron ratios, $[Zn/Fe] \approx (-0.5, 0.0)$ for stars at different $[Fe/H]$. To have a global view of these observations the reader can have a look at Fig. 4 from Skúladóttir et al. (2018).

The analytical calculations presented in the above papers to explain the observed trends, suggest that supernovae Ia (SNIa) can be responsible of such unusual low $[Zn/Fe]$ ratio. Indeed, SNIa produce large amount of iron with respect to zinc. Assuming that the low $[Zn/Fe]$ is just a consequence of the SNIa enrichment, the authors computed the predicted abundance ratios of other elements, finding a general good agreement with the measured values. The natural question is then: is there a degeneracy between the imprint of SNIa and massive primordial stars? And if so, how can we discriminate among these two different chemical enrichment channels?

To address these issues we estimate the possible chemical enrichment paths of an ISM imprinted by normal Pop II stars exploding as both core-collapse SN (SNII) and supernovae Ia (SNIa), thus adopting a very similar approach of that developed by Duffau et al. (2017) and Skúladóttir et al. (2017). To avoid including the unknown contribution from primordial stars to the chemical enrichment, we assume an initial ISM composition equal to the average abundance pattern of "normal" Galactic halo stars at $\langle [Fe/H] \rangle \approx -3$ (Cayrel et al. 2004; Yong et al. 2013). These stars, which are not enhanced in carbon, i.e. $[C/Fe] < 1.0$, have very similar abundance patterns, and indeed exhibit extremely small scatters.

Starting from these chemical abundance ratios as initial conditions, we varied the final iron-abundance within the range $[Fe/H]_{out} = [-2, -0.5]$ to compute the possible $[Zn/Fe]$ and $[X/Fe]$ abundance ratios of an ISM enriched by N_{II} core-collapse supernovae and $N_{Ia} = f_{Ia} N_{II}$ supernovae Ia, where f_{Ia} is the fraction of SNIa with respect to SNII. Such a quantity can be derived from observations and it is found to be $f_{Ia} \approx 0.1$ (e.g. Mannucci et al. 2006). By adopting the yields of Iwamoto et al. (1999), writing $M_{Fe}^{in} = M_g \times 10^{[Fe/H]_{in} - \log(M_{Fe}/M_H)_\odot}$, we computed the number of core-collapse SN required to get different iron abundances:

$$[Fe/H]_{out}^{II+Ia} = \log \left[\frac{M_{Fe}^{in} + Y_{Fe}^{II} N_{II} + Y_{Fe}^{Ia} f_{Ia} N_{II}}{M_g} \right] - \log \left[\frac{M_{Fe}}{M_H} \right]_\odot$$

where we assume a constant gas mass, M_g , as done in Duffau et al. (2017) and Skúladóttir et al. (2017). Once derived N_{II} , we computed the expected abundance ratio of the various chemical elements

$$[X/Fe]_{out}^{II+Ia} = \log \left[\frac{M_X^{in} + Y_X^{II} N_{II} + Y_X^{Ia} f_{Ia} N_{II}}{M_{Fe}^{in} + Y_{Fe}^{II} N_{II} + Y_{Fe}^{Ia} f_{Ia} N_{II}} \right] - \log \left[\frac{M_X}{M_{Fe}} \right]_\odot$$

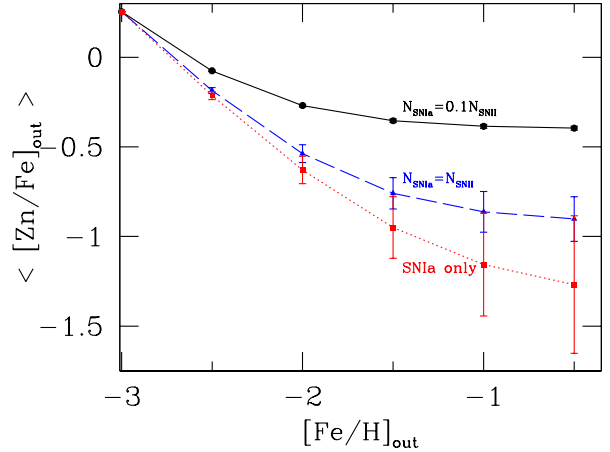


Figure 11. Average $\langle [Zn/Fe]_{out} \rangle$ of an ISM enriched by both SNII and SNIa up to different iron-abundance values $[Fe/H]_{out}$, and starting from an initial chemical composition of extremely metal-poor stars, $[Fe/H]_{in} \approx -3$ and $[Zn/Fe]_{in} \approx 0.3$ (see text and Fig. 12). The different curves refer to different SNIa-to-SNII ratios: $f_{Ia} = N_{SNIa}/N_{SNII} = (0.1, 1, > 10)$ (solid, dashed, dotted).

by varying $[Fe/H]_{out}$, f_{Ia} , and M_g . As noticed by Duffau et al. (2017) and Skúladóttir et al. (2017) these findings are independent on the assumed M_g . In Fig. 11 we show $\langle [Zn/Fe]_{out} \rangle$ with respect to $[Fe/H]_{out}$ for different choices of f_{Ia} , where the points and errorbars have been obtained by averaging among the different SNIa yields (models) by Iwamoto et al. 1999. For this reason, the larger the contribution of SNIa, the larger the errorbars. Fig. 11 shows two interesting features. First, $\langle [Zn/Fe]_{out} \rangle$ declines with increasing $[Fe/H]$, implying an overall trend that is different with respect to the $[Zn/Fe]$ plateau predicted for an ISM enriched by PISN and SNII (Fig. 7). Second, none of the models reach values $[Zn/Fe] < -1.5$, which characterise an ISM imprinted by PISN at a $\geq 90\%$ level. This is also true for the case $f_{Ia} > 10$, which is extreme and unlikely as it is equivalent to assume that *only* SNIa pollute the ISM while observations suggest $f_{Ia} = 0.1$. In conclusion, our simple estimate show that there is not apparent degeneracy between the imprint of SNIa and massive first stars.

However, around $[Fe/H] \approx -2$, i.e. where the probability to find the descendants of PISN is highest (Fig. 7), we can see that $\langle [Zn/Fe]_{out} \rangle \approx -0.5 \pm 0.3$ for all f_{Ia} , which is similar to the high $[Zn/Fe]$ abundance ratio of an ISM imprinted by PISN at a 50% level (Fig. 7, right bottom panel). How can we discriminate these different chemical enrichment channels? Fig. 12 shows the complete chemical abundance patterns we do expect when $[Fe/H]_{out} \approx -2$ for different f_{Ia} . We note that independent on f_{Ia} we have $\langle [(N, Cu, Zn)/Fe] \rangle \leq 0$, i.e. all the values are similar to the highest $[X/Fe]$ peaks of an ISM enriched by PISN at a 50% level. Yet, there are some key differences. For all f_{Ia} , $\langle [(Cr, Ni)/Fe] \rangle > 0$, while in environments enriched by PISN at a $\geq 50\%$ level we have different values depending upon the m_{PISN} . Furthermore, for the most likely and observationally constrained SNIa-to-SNII ratio, i.e. $f_{Ia} \approx 0.1$, the light elements O, S, and Si, show similar super-solar values. In conclusion, there are several elements that can allow us to discriminate among an ISM polluted by SNII and a PISN or by SNII and SNIa.

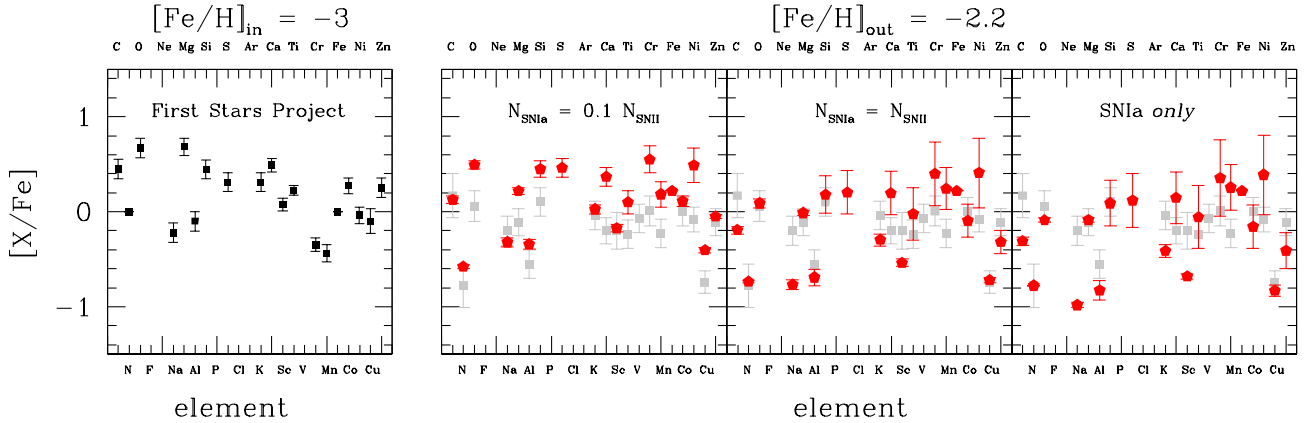


Figure 12. *Left:* chemical abundances of Galactic stars at $[\text{Fe}/\text{H}] \approx -3$, which are assumed as the initial conditions for the ISM in our calculations (see text). To derive $[X/\text{Fe}]$ we have averaged the measurements of the First Stars project sample, using NLTE results when available (Cayrel et al. 2004; Andrievsky et al. 2007, 2008; Bonifacio et al. 2009; Spite et al. 2011, 2012). For Cu we have used the results of Andrievsky et al. (2008) and for Cr the average of CrI abundances from (Cayrel et al. 2004). Errorbars show the star-to-star scatter. *Right:* chemical abundance pattern of the ISM enriched up to $[\text{Fe}/\text{H}]_{\text{out}} \approx -2.2$ with the contribution of both SNIi and SNIa (red pentagones). Errorbars represent the 1σ deviation among different SNIa models. The panels show results for different SNIa-to-SNIi ratios (see labels). Grey squares show the chemical abundance pattern of a possible PISN descendant, the star BD +80° 245, for which we measured $[\text{Fe}/\text{H}] = -2.2$ (Sec. 5).

5 BD +80° 245: THE SMOKING GUN OF A PISN EXPLOSION ?

In the following section, we suggest that the peculiar abundance pattern of the star BD +80° 245 may be explained if it has been formed from gas polluted by a primordial PISN, with $f_{\text{PISN}} \geq 0.5$. This star, with $[\text{Fe}/\text{H}] = -2.09$, was discovered as an α -poor star by [Carney et al. \(1997\)](#).

The star has been subsequently analysed by [Fulbright \(2000\)](#), based on spectra taken at Keck telescope with the HIRES spectrograph ([Vogt et al. 1994](#)), by [Ivans et al. \(2003\)](#) and [Roederer et al. \(2014\)](#). The latter two investigations, as well as the original discovery paper, are all based on spectra obtained at the McDonald Observatory with the “2d-coudé” echelle spectrograph at the 2.7m Harlan J. Smith telescope. Each of the three investigation acquired an independent spectrum. All four investigations agree, within errors, on atmospheric parameters and detailed abundances of the different elements. The two most interesting studies for our purposes are those of [Ivans et al. \(2003\)](#) and [Roederer et al. \(2014\)](#).

Both studies report a significant under-abundance of Zn with respect to iron, which is unusual. Here and in the following we transform the published abundances to our preferred solar abundance scale (see Table 1), namely $A(\text{N}) = 7.86$, $A(\text{Fe}_{\odot}) = 7.52$ ([Caffau et al. 2011](#)) and $A(\text{Cu}_{\odot}) = 4.25$, $A(\text{Zn}_{\odot}) = 4.47$ ([Lodders et al. 2009](#)). On this scale [Ivans et al. \(2003\)](#) reports $[\text{Zn}/\text{Fe}] = -0.29$, and [Roederer et al. \(2014\)](#) $[\text{Zn}/\text{Fe}] = -0.27$. [Ivans et al. \(2003\)](#) reports also an upper limit on Cu, namely $[\text{Cu}/\text{Fe}] < -1.07$ and [Roederer et al. \(2014\)](#) an upper limit on N, namely $[\text{N}/\text{Fe}] < +1.0$.

5.1 BD +80° 245: new spectra and analysis

We observed two spectra of BD +80° 245 with the SOPHIE spectrograph ([Bouchy & Sophie Team 2006](#)) on the 1.93 m telescope at Observatoire de Haute Provence, on March 16th with an integration of 466 s and March 17th 2018 with an integration of 1800 s. In both nights the meteorological observations were far from ideal and we observed through thin to thick clouds conditions. We used the high efficiency mode (HE) that provides a resolving power of $R=39000$. The radial velocities measured by the SOPHIE pipeline with a G2 mask where 4.96 km s^{-1} and 4.98 km s^{-1} respectively, in excellent agreement with the mean radial velocity measured by [Latham et al. \(2002\)](#). The S/N ratio of the coadded spectrum is 53 at 510 nm. The goal of our observations was to try to improve on the upper limits on the abundances of N and Cu, but the quality of the spectra does not allow that.

Nevertheless the SOPHIE spectrum allowed a robust determination of 12 elements, of which three are in two different ionisation stages. To derive the abundances we use the MyGIsFOS code ([Sbordone et al. 2014](#)) and a grid of synthetic spectra computed with the SYNTH code ([Kurucz 2005](#)) in its Linux version ([Sbordone et al. 2004](#)), from a grid of one-dimensional LTE, plane-parallel model atmospheres computed with version 12 of the ATLAS code ([Kurucz 2005](#)). The adopted atomic line list is described by [Heiter et al. \(2015\)](#) and the molecular lines were those compiled by R. Kurucz⁴. The results are reported in Table 1 and they are, by and large, in good agreement with those of [Ivans et al. \(2003\)](#). The small offsets of the order of 0.15 dex, for some elements, can be ascribed to the different lines and atomic parameters adopted in the two studies.

We retrieved from the Keck Observatory Archive

⁴ <http://kurucz.harvard.edu/linelists/linesmol>

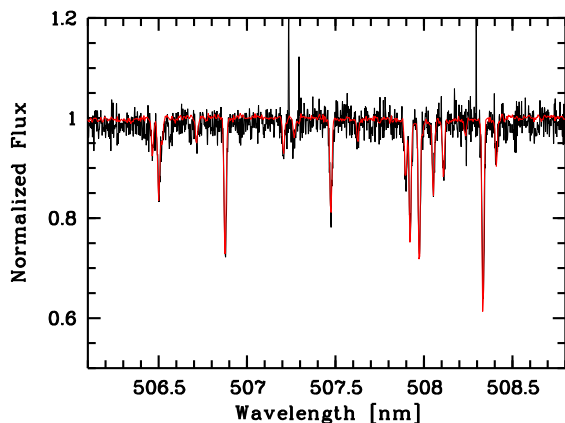


Figure 13. A portion of our SOPHIE spectrum of BD +80° 245 compared to the HIRES spectrum. The HIRES spectrum is at much higher S/N (350 to be compared to 53 of the SOPHIE spectrum in this region) and slightly higher resolution. However, the two wavelength scales are in good agreement.

(KOA⁵) one HIRES (Vogt et al. 1994) spectrum of BD +80° 245 which was available already reduced. This spectrum was observed on June 12th 2006 with a slit of 0''861, which provides a resolving power of $R=45000$. The spectral coverage is from 290 nm to 585 nm, the exposure time 1200 s and the S/N ratio at 500 nm is about 350. We are aware that the KOA extracted spectra are intended for quick look and are not guaranteed to be “science ready”, however in this case we could verify the HIRES spectrum against the SOPHIE spectrum (see Fig. 13 for an example) and convinced ourselves that both the wavelength scale and the intensity scale are free from significant systematic errors, therefore suitable for a science analysis.

There is a good agreement in the literature on the atmospheric parameters of BD +80° 245 we decided to adopt those of Ivans et al. (2003) to simplify the comparison with their results: $T_{\text{eff}} = 5225$ K $\log g = 3.00$ and a metallicity of -2.0 . We computed an ATLAS 9 model (Kurucz 2005), using its linux version (Sbordone et al. 2004) using the updated Opacity Distribution Function of Castelli & Kurucz (2003) with a 1 km s^{-1} microturbulence.

5.1.1 BD +80° 245: the key element Cu

The line of CuI at 510.5 nm cannot be detected in the HIRES spectrum, however both the UV resonance lines at 324.7 nm and 327.3 nm can be readily detected as shown in Fig. 14 and Fig. 15. These lines are known to suffer from strong NLTE effects (Andrievsky et al. 2018; Korotin et al. 2018), we therefore computed NLTE profiles to determine the Cu abundances and these profiles are shown in Fig. 14 and Fig. 15. The two lines provide a consistent Cu abundance and the average is $A(\text{Cu}) = 1.29 \pm 0.03$ dex, or $[\text{Cu}/\text{Fe}] = -0.75$. We verified that this Cu abundance is consistent with the non-detection of the CuI 510.5 nm line. Bonifacio et al. (2010) have also shown that the UV resonance lines are strongly affected by granulation effects that go in the opposite direction: 3D corrections to the Cu abundance are always neg-

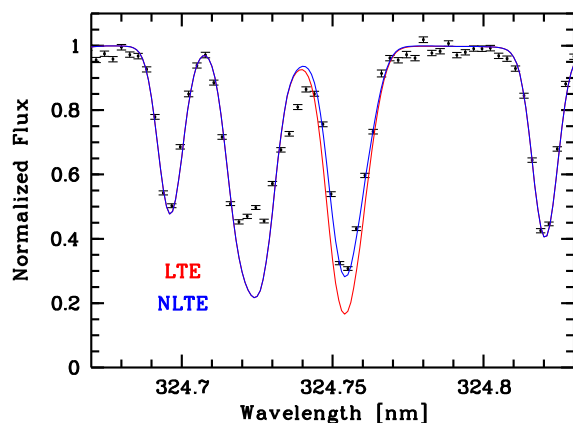


Figure 14. The HIRES spectrum of BD +80° 245 in the region of the CuI resonance line at 324.7 nm (dots). Two synthetic spectra are shown for an ATLAS 9 model with $T_{\text{eff}} = 5225$ K $\log g = 3.00$ and $[\text{M}/\text{H}] = -2.0$. The red line corresponds to the LTE computation and the blue line to the NLTE computation. In both cases $A(\text{Cu}) = 1.32$.

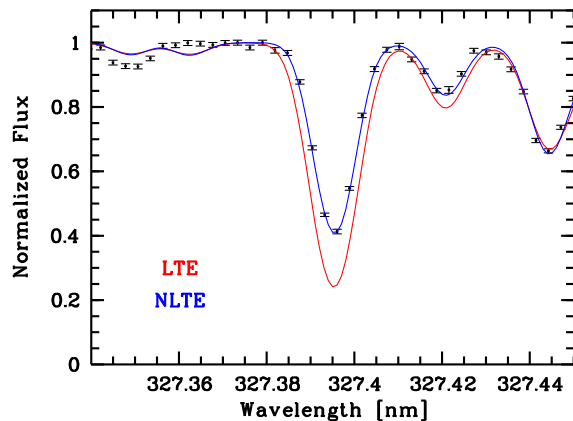


Figure 15. The same as in Fig. 14 for the CuI resonance line at 327.3 nm. Synthetic spectra assume $A(\text{Cu}) = 1.26$.

ative, while NLTE corrections are always positive. At the present time we are not able to perform a full 3D–NLTE computation, but we can gain some insight from the work of Roederer & Barklem (2018). Since CuII is the majority species in the atmospheres of these stars, we can assume that its lines form in conditions that are close to LTE, thus the difference between the LTE abundance of CuII and that of CuI can be taken as a proxy of the NLTE correction for CuI. In their figure 3 they show how for their sample of stars this proxy follows the general trend of the NLTE corrections of Andrievsky et al. (2018), being somewhat lower. From this comparison we can expect that the full 3D–NLTE correction is smaller than the 1D NLTE. The consequence for BD +80° 245 is that our NLTE Cu abundance is probably an upper limit to the true 3D–NLTE abundance. Thus our conclusion that Cu is strongly underabundant with respect to Fe in this star is robust against NLTE and 3D effects.

⁵ <https://koa.ipac.caltech.edu/>

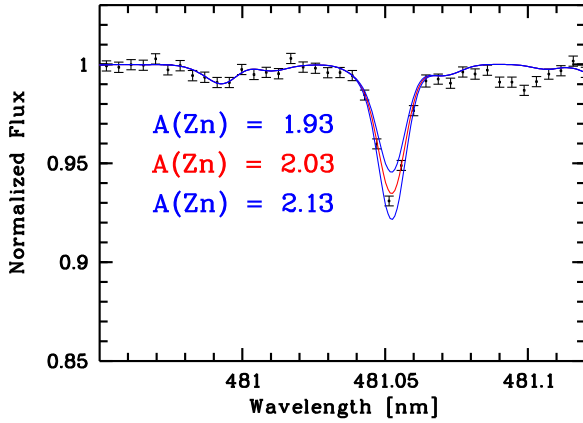


Figure 16. The same as in Fig. 14 for the ZnI line at 481.0 nm (dots). The red line corresponds to the abundance determined by us with a χ^2 fit, and the two blue lines correspond to the ± 0.1 dex variation in the Zn abundance.

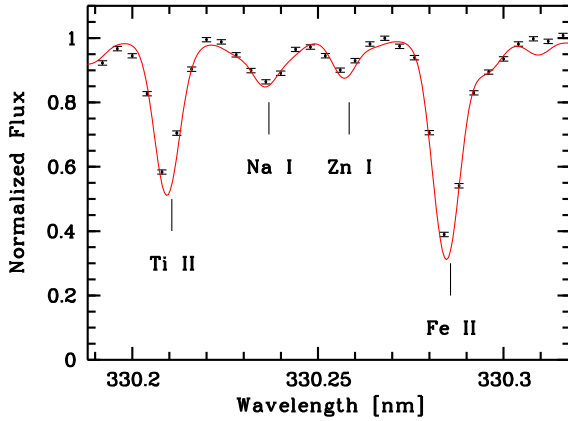


Figure 17. The same as in Fig. 14 for the ZnI line at 330.2 nm. Synthetic spectra assume $A(\text{Zn}) = 2.21$.

5.1.2 *BD +80° 245: the key element Zn*

The line of ZnI at 481.0 nm can be readily detected in the HIRES spectrum, as shown in Fig. 16. To derive the Zn abundance we use a χ^2 fitting of synthetic line profiles and derive $A(\text{Zn})=2.03$, this is in excellent agreement with the values derived by both [Ivans et al. \(2003\)](#) and [Roederer et al. \(2014\)](#). The difference of 0.06 dex in our Zn abundance and that of [Ivans et al. \(2003\)](#) is due to both the different log gf assumed for this line (-0.137 assumed by us and -0.170 assumed by [Ivans et al. \(2003\)](#)) and to the slightly different equivalent width. Our fitted equivalent width is 0.67 pm in excellent agreement with [Roederer et al. \(2014, 0.65 pm\)](#). In addition we could detect the ZnI doublet lines at 330.2 nm in the HIRES spectrum. Our best fit is shown in Fig. 17 and it provides $A(\text{Zn})=2.21$. The region is rather crowded and the continuum is difficult to define, and it is necessary to model also the neighbouring lines. For this reason this line is probably less reliable than the 481.0 nm line. Nevertheless the two lines provide consistent abundance the straight mean of the two is $A(\text{Zn}) = 2.12$ dex with a σ of 0.09 dex. The Zn and Fe abundances should be fairly immune both to departures from LTE ad from 3D effects at the metallicity of *BD +80° 245*. The departures from LTE for

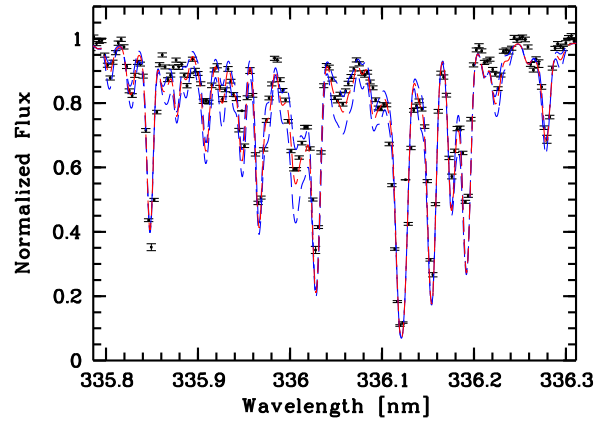


Figure 18. The HIRES spectrum of *BD +80° 245* in the region of the NH band at 336 nm (dots) and the best fit synthetic spectrum corresponding to $A(\text{N}) = 4.87$ (solid red line). We also show synthetic spectra compute with ± 0.2 dex of our best fit N abundance (dashed blue lines) and take this as error estimate.

Zn have been studied by [Takeda et al. \(2005\)](#) and any correction is expected to be less than 0.1 dex. This is also supported by the recent study of [Roederer & Barklem \(2018\)](#), who measured both ZnI and ZnII lines in a set of stars. As for Cu, on the assumption that the lines of the majority species in the stellar atmosphere, ZnII, are formed under condition that are close to LTE, then the difference of abundance between ZnII and ZnI can be taken as a proxy of the NLTE correction that has to be applied to the abundances derived from the ZnI. For all the sample of [Roederer & Barklem \(2018\)](#) the abundances derived from the two ions are very similar, implying small NLTE corrections, in agreement with the computations of [Takeda et al. \(2005\)](#). For Fe the NLTE corrections at $[\text{Fe}/\text{H}] \approx -2.0$ are expected to be less than 0.1 dex for giants with $\log g \geq 2.0$ ([Mashonkina et al. 2016](#)). [Duffau et al. \(2017\)](#) studied the effects of granulation (3D effects) on Zn, for solar metallicity and for -1.0, concluding that these effects are small and the $[\text{Zn}/\text{Fe}]$ ratio should not be strongly affected.

5.1.3 *BD +80° 245: the key element N*

The HIRES spectrum also allowed us to detect the NH band at 336 nm, as shown in Fig. 18. Our best fit synthetic spectrum provides $A(\text{N})=4.86$, or $[\text{N}/\text{Fe}] = -0.79$. To fit the whole region we assumed the oxygen abundance derived from the OH lines (see next Section) and the abundance of Ti and Sc provided by [Ivans et al. \(2003\)](#). The uncertainty in this fitting is due to the continuum placement and we estimate it to be 0.2 dex. The NH band is subject to granulation corrections, which always decrease the abundance with respect to that derived from a 1D analysis (see e.g. [Bonifacio et al. 2013](#); [Collet et al. 2018](#), and references therein). We have not yet performed this computation, since it is computationally demanding nor could we find computations in the literature for stars of similar atmospheric parameters. For the purpose of the present investigation we simply note that since the 1D analysis implies that N is under-abundant with respect to iron, a 3D analysis will result in an even lower N abundance.

5.1.4 BD +80° 245: oxygen determination

We could detect many OH lines of the $A^2\Sigma^+ - X^2\Pi$ system, that allowed us to determine the oxygen abundance in BD +80° 245. We used wavelengths from Stark et al. (1994) and $\log gf$ values calculated from the theoretical lifetimes of Goldman & Gillis (1981). Note that these are almost identical to the more recent theoretical calculations of Gillis et al. (2001). The only exception was the line at 311.0780nm for which we adopted $\log gf = -3.274$ from the updated lists of R. Kurucz⁶. Using a synthetic spectrum as a guideline we selected only lines that were either clean or mildly blended. In some cases two or more OH lines were blended together and we fit the whole feature. When a line appeared in two adjacent echelle orders we took two independent measures. In total we have 46 independent measures of oxygen that provide a mean abundance $A(O) = 6.85$ with a line-to-line scatter of 0.11. This corresponds to $[O/Fe]=+0.30$, and it is lower than the mean ratio in Galactic stars at these $[Fe/H]$. The OH lines are also known to be affected by granulation effects (see e.g. Gallagher et al. 2017; Collet et al. 2018, and references therein). We apply the correction computed by González Hernández et al. (2010), which amounts to -0.25 dex, implying $A(O)=6.60$, or $[O/Fe]=+0.06$.

5.1.5 BD +80° 245: age and orbit determination

The second data release of the Gaia mission (Gaia Collaboration et al. 2016, 2018; Arenou et al. 2018) has provided a very accurate parallax for this star 4.296 ± 0.0270 mas, which allows us to have an accurate measurement of its luminosity. In Fig. 19 we show the Hertzsprung-Russel diagram with the position of the star compared to a set of PARSEC isochrones (Bressan et al. 2012) with $Z = 0.000152$ and ages between 1 Gyr and 13.5 Gyr. We assumed an error of 150 K on the effective temperature of the star and draw 3σ error bars in the diagram. The position of the star is anomalous, it appears too cool for its luminosity. An increase in T_{eff} would also imply an increase in metallicity, which also would help to make the position of this star more compatible with the isochrones. An increase in metallicity moves the isochrones towards cooler temperatures in this diagram. It may also be that the position of this star is due to its peculiar chemical composition. The fact that the star does not show any radial velocity variations does not support the hypothesis that the star is a binary. In spite of its anomalous position we can say that it certainly points towards a very old age. BD +80° 245 was probably born only a few 10^8 years after the Big Bang.

Finally, we used the Gaia parallax and proper motions, together with our measured radial velocity, to compute a Galactic orbit for BD+80° 245. To this end we used GravPot16 (Fernández-Trincado 2019) and its default gravitational potential, based on the Besançon model⁷. The orbit of BD +80° 245 is a typical “halo” orbit: highly eccentric ($e = 0.46$), maximum height above the Galactic plane of 13 kpc, apocentric distance of 14.6 kpc and a slow retrograde

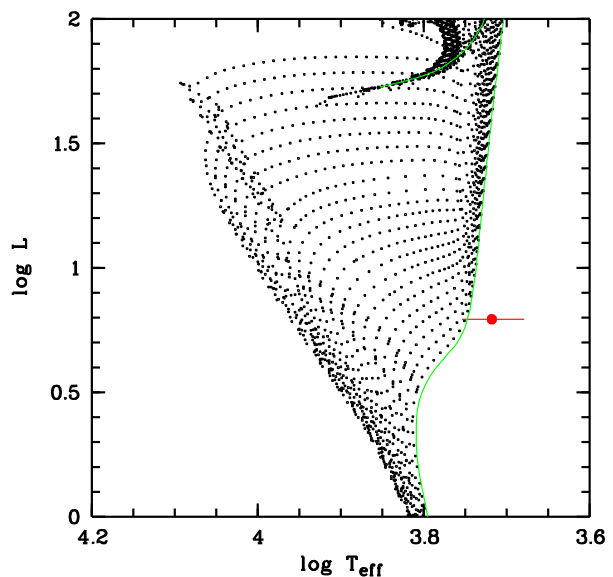


Figure 19. PARSEC isochrones (Bressan et al. 2012) with $Z = 0.000152$ and ages between 1 and 13.5 Gyr. The green isochrone corresponds to 13.5 Gyr. The red point shows the position of BD +80° 245 in this diagram, and error bars correspond to 3σ errors in T_{eff} and parallax.

rotation. This is compatible both for a star accreted from a satellite galaxy, and with an “in situ” halo star.

5.2 BD +80° 245: model comparison

In conclusion, BD +80° 245 can be a descendant of very massive first stars since: (i) it is likely a very ancient star and (ii) it exhibits under-abundances of the three key elements, N, Cu and Zn, which are consistent with the abundance ratios shown in Fig. 7 for $f_{\text{PISN}} = 0.5$. We can thus directly compare the chemical abundance pattern of BD +80° 245 with our model predictions for an ISM imprinted by very massive first stars and determine the best fitting model. To this end we computed the χ^2 distribution normalized to the degrees of freedom, $\chi^2_{\nu} = \chi^2 / (N - M)$ (e.g. see Ishigaki et al. 2018), where N is the number of data points to be fitted, M the number of model free-parameters (f_*/t_{dil} , f_{PISN} , t_{popII} , m_{PISN}) and χ^2 has been computed as:

$$\chi^2 = \sum_{i=1}^N \frac{([X_i/Fe]_{\text{obs}} - [X_i/Fe]_{\text{th}})^2}{(\sigma_{[X_i/Fe]_{\text{obs}}}^2 + \sigma_{[X_i/Fe]_{\text{th}}}^2)}. \quad (14)$$

In the above expression $[X_i/Fe]_{\text{obs}}$ is the observed abundance ratio of the element i with respect to iron and $\sigma_{[X_i/Fe]_{\text{obs}}}^2 = \sigma_{X_{i,\text{obs}}}^2 + \sigma_{Fe,\text{obs}}^2$ the associated observational error. These values are reported in Table 1 for all measured elements. For Na, Al, Si, K, V, Mn, Co, we used the values measured by Ivans et al. 2004 and we estimated $\sigma_{[X_i/Fe]_{\text{obs}}}^2 = \sigma_{Al,\text{obs}}^2 + \sigma_{Fe,\text{obs}}^2 \approx 0.15$. The terms $[X_i/Fe]_{\text{th}}$ in eq. 14 represent the theoretical chemical abundance ratios of an ISM imprinted by both a PISN and normal Pop II stars. Given the large yield uncertainties among different models for Pop II stars (Fig. 10, left panels) we assume $\sigma_{[X_i/Fe]_{\text{th}}}^2 = 0.5$ for all elements. The results of the χ^2_{ν} distribution for all our model parameters is reported in Ap-

⁶ <http://kurucz.harvard.edu/molecules/oh/ohaxupdate.ac>

⁷ <https://fernandez-trincado.github.io/GravPot16/index.html>

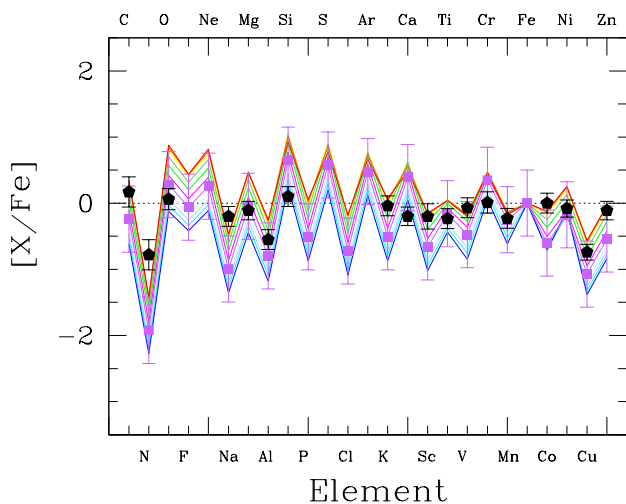


Figure 20. Comparison between the chemical abundance pattern of BD +80° 245 inferred from spectroscopic observations (black circles with errorbars, see text and Table 1) and the best fitting model parameters: $f_*/f_{\text{dil}} = 10^{-4}$, $f_{\text{PISN}} = 0.5$, and $t_{\text{popII}} = 30$ Myr. The different colours/curves show the chemical abundance pattern predicted for different PISN masses (see Fig. 3). Violet squares with errorbars show the best-fitting model, which corresponds to $m_{\text{PISN}} = 223M_{\odot}$.

pendix A. Our analysis show that models with $f_{\text{PISN}} = 0.5$, $t_{\text{popII}} = 30$ Myr, and $f_*/f_{\text{dil}} = 10^{-4}$, are those that best-fit the abundance pattern of BD +80° 245, providing $\chi^2_{\nu} < 2$ in the overall PISN mass range. In Fig. 20 the chemical abundance pattern of all these models are compared with BD +80° 245. Our best fitting-model (violet points with errorbars) corresponds to a PISN mass $m_{\text{PISN}} = 223M_{\odot}$, which gives $\chi^2_{\nu} = 0.99$. As expected, the agreement between this model and BD +80° 245 is quite good, thus suggesting that this rare star is really a PISN descendant. It is worth noticing that although $f_*/f_{\text{dil}} = 10^{-4}$ is typical of mini-halos (see Sec. 7.1) we cannot exclude that BD +80° 245 has been polluted by more than one PISN, a possibility that we did not explore with our current modelling. On the contrary, it is unlikely that BD +80° 245 formed out of an ISM enriched by both SNIi and SNIa as the star is very ancient and the models provide a partial agreement to the data (see Fig. 12). Only by assuming an equal contribution of SNIa and SNIi, $f_{\text{ia}} = 1$, we obtain a partial agreement with the data (middle panel in Fig. 12). Yet, even this model largely under-estimates the $[(\text{C}, \text{Na}, \text{K}, \text{Sc})/\text{Fe}]$ abundance ratios and it overestimates $[(\text{Ni}, \text{Cr})/\text{Fe}]$. In conclusion, all available data suggest that BD +80° 245 might really be the first evidence of a PISN descendants.

6 OBSERVATIONAL PROSPECTS

In Sect. 5 we argued that BD +80° 245 has all the chemical signatures that allow to single out a true descendant of a PISN. As suggestive as this may be, a single star cannot strongly constrain the PISN pollution models. We therefore believe it is very important to search for other stars with the PISN chemical signature, both in order to be sure that this is not an exception, and, if such stars are found, to know what is their frequency. The latter would in fact constrain

the number of PISN exploding in the early Galaxy and thus the IMF of Pop III stars (e.g. de Bennassuti et al. 2017). Aoki et al. (2014) claimed that SDSS J001820.5–093939.2 is another such PISN descendant. Their claim is based mainly on the low α/Fe ratios in this star, however this signature could also indicate a prompt enrichment of the ISM by SNIa as suggested by Ivans et al. (2003) for BD +80° 245. Furthermore it is now becoming clear that there is a population of low- α stars at low metallicity (Caffau et al. 2013; Bonifacio et al. 2018b). Are all of these PISN descendants? Some fraction of them? SDSS J001820.5–093939.2 could well be a PISN descendant, however unfortunately, it is too faint to allow a measurement of the key elements, N, Cu and Zn.

6.1 Looking for the killing elements

Our simple model, and the study of BD +80° 245 can give us some insight into what stars and lines we should look for. The strongest spectral features to look for are the CuI UV resonance lines and the NH 336 nm band as shown in Fig. 14, 15 and 18. The penalty is that observing in the UV is difficult from the ground and one needs a fairly high resolution ($R \approx 20000$). For all three features a resolution that is one half of that of the spectra analysed here is sufficient and the S/N ratio can be as low as 30.

However the real problem is that as of today, to our knowledge, there are only 5 spectrographs that can observe at these wavelengths with a sufficient, or barely sufficient resolution and they are all installed on 6 to 10 m class telescopes. At the VLT there are UVES (Dekker et al. 2000) and X-Shooter (Vernet et al. 2011). The latter only if one could observe with a $0''.3$ slit or an image slicer of the same width, currently neither is available. There is HIRES (Vogt et al. 1994) at Keck, as used in this paper and there is HDS (Noguchi et al. 2002) at Subaru. It is unrealistic to conduct a survey of a large number of stars with any of these instruments, because of the high pressure on the telescopes and because they all operate in single object mode. Probably the most promising instrument is the fifth one: IMACS+MOE (Bigelow et al. 1998; Sutin & McWilliam 2003) on the Magellan telescope. This provides a resolving power $R \sim 20000$ covering the spectral regions relevant for N and Cu and has a multi-object capability, over a field-of-view of $15' \times 15'$. This field of view is interesting, but, as we shall see below, probably not sufficient to conduct a survey searching for PISN descendants.

None of the wide-field multi-object spectrographs that either exist or are being built has access to the far UV region necessary for this study. This is due to a combination of the difficulty of having a fibre-fed spectrograph that is efficient in the UV and of the difficulty of having a wide-field high resolution multi-slit spectrograph. IMACS+MOE here is the exception and it would be interesting to see if the concept could be transferred to a really wide field, of the order of one degree diameter.

So in spite of the fact that the features of N and Cu are stronger, it turns out that the most promising candidate to search for true PISN descendants is Zn. One needs to have a S/N ratio and resolving power sufficient to measure the ZnI line at 481.0 nm when it has an equivalent width of 0.5 to 1.0 pm. Clearly one would gain by observing stars cooler

Table 1. Chemical abundance ratios of BD+80°245 derived with our analysis. The lines used to determine the different chemical elements are reported in Appendix B (Tables 2-10).

Ion	A(X_{\odot})	A(X)	uncertainty	[X/H]	[X/Fe]	Δ [X/Fe]	N lines	spectrum	Comment
C	8.50	6.46	0.20	-2.045	+0.17	0.23		HIRES	G-band
N	7.86	4.86	0.20	-3.00	-0.78	0.23		HIRES	NH band 336 nm
O	8.76	6.60	0.11	-2.16	+0.06	0.16	43	HIRES	OH, 3D corrected
MgI	7.54	5.20	0.08	-2.33	-0.11	0.01	3	SOPHIE	
CaI	6.33	3.91	0.08	-2.42	-0.2	0.14	18	SOPHIE	
ScII	3.10	0.68	0.15	-2.42	-0.2	0.19	5	SOPHIE	
TiI	4.90	2.39	0.08	-2.51	-0.29	0.14	9	SOPHIE	
TiII	4.90	2.50	0.10	-2.40	-0.18	0.15	25	SOPHIE	
CrI	5.64	3.27	0.07	-2.37	-0.15	0.16	11	SOPHIE	
CrII	5.64	3.60	0.12	-2.04	+0.17	0.16	5	SOPHIE	
FeI	7.52	5.31	0.11	-2.21			150	SOPHIE	
FeII	7.52	5.30	0.06	-2.22			23	SOPHIE	
NiI	6.23	3.94	0.06	-2.30	-0.08	0.13	14	SOPHIE	
CuI	4.25	1.29	0.03	-2.96	-0.74	0.12	2	HIRES	NLTE
ZnI	4.47	2.14	0.09	-2.33	-0.11	0.14	2	HIRES	
SrII	2.92	-0.12	0.17	-3.04	-0.82	0.2	2	SOPHIE	
YII	2.21	-1.25	0.20	-3.46	-1.24	0.23	1	SOPHIE	
BaII	2.17	-1.93	0.25	-4.1	-1.89	0.27	3	SOPHIE	

than BD +80° 245 since for a given Zn abundance the line becomes stronger. However the isochrones in Fig. 19 show how the Red Giant Branch climbs almost vertical and the cool giants of $T_{\text{eff}} \sim 4000$ K are found only at the RGB tip and thus are a very rare population.

6.2 Zn surveys to catch the PISN descendants

There are two instruments that can conduct a survey of Zn abundances in metal-poor stars to catch the descendants of very massive first stars: HERMES at the AAT (Barden et al. 2010) and WEAVE at the WHT (Dalton et al. 2016). Unfortunately 4MOST on Vista (de Jong et al. 2016) will not cover the ZnI 481.0 nm line at high resolution. Yet, we should note that 4MOST might also help in finding more PISN descendants since it will easily measure the [Sc/Ca] ratio, which is predicted to be extremely low in PISN-enriched environments (e.g. Fig. 2).

6.2.1 The HERMES and WEAVE spectrographs

The HERMES spectrograph uses the 2dF corrector and positioner on the AAT (Taylor et al. 1997) to deploy 400 fibers over a field of view with 2 degrees diameter. It was commissioned at the end of 2013 (Sheinis et al. 2014) and has been operating for the last 5 years. One of the main surveys being conducted with this instrument is the Galactic Archaeology with HERMES (GALAH) survey (De Silva et al. 2015). The survey has recently published its second data release (Buder et al. 2018) that contains 342 682 stars and derived atmospheric parameters and chemical abundances. It normally observes stars in the magnitude range $12 < V < 14$ with no colour selection. This data set contains Zn abundances for 248 993 stars all of which with $[\text{Fe}/\text{H}] > -2.0$. There are no stars with $[\text{Fe}/\text{H}] < -1.5$ that have a $[\text{Zn}/\text{Fe}]$ that is significantly below the Solar abundance.

WEAVE should arrive on the sky at the end of 2019 and will deploy about 1000 fibres over a field of view of two

degrees of diameter. The fibers feed a two arms spectrograph (Rogers et al. 2014) that can be operated either in a low resolution mode (R \sim 5000) or in a high resolution mode (R \sim 20000). The high resolution mode covers two non contiguous intervals of about 60 nm in the blue and 90 nm in the red. The red interval is fixed and is 595 nm to 685 nm. In the blue one can chose between two gratings which cover either the 404 nm to 465 nm (blue grating) range or the 473 nm to 545 nm range (green grating). Only the observations with the green grating are relevant to determine the Zn abundance, since it covers the 481.0 nm line.

6.2.2 The observational strategy

In order to understand what could be observed with HERMES and WEAVE we used the galaxia (Sharma et al. 2011) implementation of the Galaxy Besançon model (Robin et al. 2003). We selected as potential targets giants stars with $T_{\text{eff}} < 5300$ K and $\log g \leq 3.0$. If we consider a GALAH-like magnitude selection $12 < V < 14.5$, with a metallicity in the interval $-1.5 \leq [\text{Fe}/\text{H}] \leq -2.5$ the number of candidate stars per square degree is on average one for all Galactic latitudes $|b| > 40^\circ$. As we go to lower Galactic latitudes the number increases and is of the order of two, with about 1 star out of four coming from the thick disc. Up to now most of GALAH observations have been taken at $|b| < 40^\circ$, it is thus not surprising that there is a lack of metal-poor stars.

The WEAVE Galactic Archaeology survey aims at high resolution observations in the magnitude range $13 < V < 16$. With this magnitude range and the above conditions on T_{eff} , $\log g$ and metallicity the number of targets per square degree is of the order of three for $|b| > 40^\circ$ and increases to about six in the range $20 < |b| \leq 40^\circ$, due to the contribution of the metal-weak thick disc.

Considering that both HERMES and WEAVE spectrographs have a field of view larger than three square degrees, if we push observations down to $V < 16$ we can expect about

nine giants in the metallicity range $-1.5 \leq [\text{Fe}/\text{H}] \leq -2.5$ for each pointing. On the assumption that a 1h integration allows to reach a high enough S/N ratio to measure Zn and that we can do 7 such exposures per night we would need of the order of 160 nights of observations on either or both telescopes. If we can pre-select the metal-poor giants without need of taking spectra, such a survey could be executed as a parasite survey, since it needs very few fibres (with respect to the total number of fibres available), while the majority of the fibres is dedicated to other targets. Such a pre-selection is indeed possible. The Gaia parallaxes are already available for all stars with $V < 16$ and can be effectively used to select only giant stars. This allows to filter out nearby K dwarfs that have the same colours of K giants and are metal-rich. The temperature range can be easily selected from a colour, and now Gaia provides homogeneous $G_{BP}-G_{RP}$ photometry that is well adapted for the purpose.

The most difficult part is the iron-abundance selection. However in the northern hemisphere the Pristine Survey (Starkenburger et al. 2017) should be able to select stars with $[\text{Fe}/\text{H}] < -1.5$ and in the southern hemisphere the same can be accomplished with the SkyMapper Survey (Keller et al. 2007). Both photometric surveys can be usefully complemented by the Gaia spectrophotometry. Furthermore, when the Gaia RVS photometry becomes available it has been shown that it can provide a very powerful metallicity diagnostic for F,G and K stars (Bonifacio et al. 2018a). It thus seems that a pre-selection of metal-poor giants is indeed possible. An investment of 160 nights, spread over several years and two telescopes seems achievable. Especially considering that the strategy we are proposing is little intrusive in the sense that it requires only few fibres to be allocated, while the instrument is conducting other surveys. It is more intrusive for WEAVE than for HERMES, for two reasons: in the first place it requires that the high resolution mode be used, in the second place it requires the use of the green grating. The green grating is good for Zn and for metal-rich stars, while the blue grating is optimized for metal-poor stars. Independently of the measure of Zn there is an interest for WEAVE to switch to the green grating when going at lower galactic latitudes.

In all those cases targeting 10 to 20 candidate metal-poor giants selected by photometry and parallax would allow to assemble a significative sample of Zn measurements in metal-poor giants. If stars with low $[\text{Zn}/\text{Fe}]$ are found, the strategy would be to go to an 8-10m class telescope and observe the UV to derive N and Cu abundances and have the confirmation that the star is a PISN descendant.

7 SUMMARY AND DISCUSSION

The lack of a convincing chemical signature from massive first stars exploding as Pair Instability SN (PISN) is at odds with predictions from cosmological simulations, which find that Pop III stars with masses $m_{\text{popIII}} > 150M_{\odot}$ should have formed. All ideas proposed to explain these negative results underline the *challenges* in finding the rare PISN descendants: it is very likely that these stars are less frequent than the descendants of lower mass Pop III stars (e.g. Cooke & Madau 2014 de Bannassuti et al. 2017, Chiaki et al. 2018). Furthermore, they likely appear at higher metallicities,

$[\text{Fe}/\text{H}] \approx -2$, where they only represent $< 0.01\%$ of the total stellar population (Salvadori et al. 2007; Karlsson et al. 2008; de Bannassuti et al. 2017). New observational strategies are thus required to search for these elusive stellar fossils.

With this aim, we developed a novel, simple, and generic parametric study to define what are the key chemical abundance ratios we should look for to quickly identify the PISN signature. We first investigated what are the chemical properties of an inter stellar medium (ISM) imprinted by a single PISN. Indeed, state-of-the-art hydro dynamical simulations of the first star-forming systems find that typically there is only one star per mini-halo, and that the probability to form Pop III stars with different masses is roughly constant (e.g. Hirano et al. 2014, 2015). To make a general study and account for the different cosmological scenarios (e.g. star-forming mini-halos vs more massive Ly α -cooling systems, in situ vs external metal enrichment) we modelled the chemical enrichment as a function of the unknown star-formation efficiency, f_* , and dilution factor, f_{dil} , which quantifies the effectively fraction of metals injected into the ISM and of the gas used to dilute them (Fig. 1, Sec. 2.1 and 2.2). If several PISN are formed, e.g. in more efficiently star-forming Ly α -cooling halos, we simply assume that they all have the same mass.

We found that the ISM Fe-abundance depends upon f_*/f_{dil} (eq. 3), while its abundance pattern is independent from both free parameters (eq. 4). The key results for an ISM only imprinted by PISN with a single mass, m_{PISN} , can be summarised as follow:

- for *all free parameters* $Z_{\text{ISM}} > 10^{-3}Z_{\odot} > Z_{\text{cr}}$, which implies that normal Pop II stars can promptly form,
- yet, depending upon f_*/f_{dil} and m_{PISN} , we have an ISM enriched in the broad range, $-4 < [\text{Fe}/\text{H}] < 1$;
- similarly, an ISM imprinted by PISN with different m_{PISN} show a very large variety of $[\text{X}/\text{Fe}]$;
- *independent on all free parameters*, there is an under-abundance of the key elements $[(\text{N}, \text{F}, \text{Cu}, \text{Zn})/\text{Fe}] < -1$.

Searching for the lack of N, F, Cu, and Zn with respect to Fe might then be an effective way to *pre-select* stellar candidates 100% enriched by the chemical product of PISNe. However, stars polluted by PISN only, i.e. truly second-generation stars, are predicted to be extremely rare (e.g. Salvadori et al. 2007; Karlsson et al. 2008; de Bannassuti et al. 2017, Chiaki et al. 2018). We then investigated if the under-abundance of these four key elements is preserved in an ISM *also* polluted by subsequent generation of Pop II stars, which rapidly evolve as normal core-collapse SN (SNII). By limiting our investigation to ISM with a metal mass fraction injected by PISN $\geq 50\%$ of the total mass, i.e. $f_{\text{PISN}} \geq 0.5$, we were able to derive simple expressions for both the final ISM metallicity and chemical abundance ratios. In particular, we find that $[\text{X}/\text{Fe}]$ *solely* depends upon the fraction of metals from PISN, f_{PISN} , the PISN mass, m_{PISN} , and the time passed since the Pop II formation, t_{popII} , which sets the mass of SNII contributing to chemical enrichment. Our results show that after the formation and evolution of normal Pop II stars, an ISM imprinted by a single PISN evolves as follow:

- the longer t_{popII} the more uniform $[\text{Fe}/\text{H}]$ among different m_{PISN} , i.e. $[\text{Fe}/\text{H}]$ shrinks towards higher values;
- the $[\text{Fe}/\text{H}]$ homogeneity increases for larger Pop II contribution (lower f_{PISN}) reducing the $[\text{X}/\text{Fe}]$ scatter and hence the signature of PISN with different masses;
- independent of f_{PISN} the most likely $[\text{Fe}/\text{H}]$ of an ISM imprinted by PISN at a $> 50\%$ level is $[\text{Fe}/\text{H}] \approx -2$;
- *independent on all free parameters* the under-abundance of the key elements is preserved: $[(\text{N}, \text{Cu}, \text{Zn})/\text{Fe}] < 0$.

After checking that the choice of different Pop II yields (including “hypernovae”) does not affect our findings we firmly concluded that $[(\text{N}, \text{Cu}, \text{Zn})/\text{Fe}]$ are “killing element” ratios whose under-abundance reveals the unique signature from very massive first stars. Armed with these knowledge we explored literature data to pinpoint the the PISN descendants. By searching for stars at $[\text{Fe}/\text{H}] \approx -2$ with $[(\text{N}, \text{Cu}, \text{Zn})/\text{Fe}] < 0.0$ we identified as a possible candidate the star BD $+80^\circ 245$, which was first discovered by Carney et al. (1997) and subsequently observed at high resolution by several authors (Fulbright 2000; Ivans et al. 2003; Roederer et al. 2014). We acquired two new spectra of BD $+80^\circ 245$ with the SOPHIE spectrograph, which allowed us to determine 12 different chemical elements, and re-analysed the high-resolution spectra from the Keck archive. Our analysis and model comparison allowed us to conclude that BD $+80^\circ 245$ is likely a smoking gun of a PISN explosion. In fact:

- $[\text{N}/\text{Fe}] = -0.79$, $[\text{Cu}/\text{Fe}] = -0.75$, and $[\text{Zn}/\text{Fe}] = -0.12$, consistent with an ISM of formation imprinted by PISN at 50% level;
- the overall chemical abundance pattern is in good agreement ($\chi^2_\nu = 0.99$) with our $f_*/f_{\text{dil}} = 10^{-4}$ model for an ISM equally polluted by Pop II stars with masses $\geq 8M_\odot$ (i.e. evolving on a time-scale $t_{\text{popII}} \approx 30$ Myr) and a single PISN with $m_{\text{PISN}} = 233M_\odot$;
- conversely, it cannot be explained with an enrichment driven by Pop II stars and SNIa.

Our working hypotheses, driven by state-of-the-art numerical simulations of the first star-forming systems (e.g. Hirano et al. 2014, 2015), are the following: 1) the probability to form first stars with different masses is flat; 2) in each mini-halo only one PISN forms⁸ By relaxing the first hypothesis, e.g. by assuming a decreasing probability to form more massive first stars, we might obtain that models that predict an enrichment driven by one PISN and several *primordial* core-collapse SN with masses $> 8M_\odot$ still provide a good match of BD $+80^\circ 245$. By relaxing the second one, we might realise that the abundance pattern of BD $+80^\circ 245$ is also well-fitted by models that account for an imprint by more PISNe, which have different masses. In spite of these possibilities, which we plan to investigate in future studies, we can ultimately conclude that BD $+80^\circ 245$ seems to be the first convincing example of a star imprinted *also* by very massive first stars. Ultimately, BD $+80^\circ 245$ probes that primordial stars exploding as Pair Instability SN should have existed. With current facilities the best strategy to identify

more of these very rare PISN descendants is to perform Zn surveys, which are achievable with both WEAVE and HERMES spectrographs. But where should we look for in order to maximise the probability to find the rare PISN descendants?

7.1 Were should we look for PISN descendants?

Our parametric study provide general (and hence very robust) results for the under-abundance of the three killing elements and predicts that the most likely iron abundance over the whole parameter space is $[\text{Fe}/\text{H}] \approx -2$. Yet, the typical $[\text{Fe}/\text{H}]$ values are predicted to vary in a broad range depending upon f_*/f_{dil} (Fig. 2), which should reflect different hosting halo properties (Fig. 1).

To gain insights on the environments of formation of very massive first stars and hence on the actual location of their descendants and typical $[\text{Fe}/\text{H}]$, we need to link our free parameters to the properties of star-forming halos. To this end we should assume a cosmological model and we will hereafter refer to the Λ CMD cosmology. In this scenario the first stars are predicted to form in low-mass primordial mini-haloes, with total mass $M \approx 10^{6-7}M_\odot$ and gas virial temperature $T_{\text{vir}} \leq 10^4$ K (e.g. Bromm & Yoshida 2011; Bromm 2013). These low-mass objects cool-down their gas via H_2 molecules, which are easily photo-dissociated by Lyman Werner photons. This makes mini-halos inefficiently star-forming systems meaning that their star-formation efficiency is much lower than the one of more massive (Ly α -cooling) halos. Recently, de Bennassuti et al. (2017) demonstrated that the semi-empirical formula proposed by Salvadori & Ferrara (2009) provides an excellent tool to evaluate the reduced star-formation efficiency of mini-haloes with respect to Ly α -cooling systems. The formula reads:

$$f_* = \frac{2 \times f_*^{\text{Ly}\alpha\text{-cool}}}{[1 + (2 \times 10^4 \text{K}/T_{\text{vir}})^3]} \quad (15)$$

and can be used to link f_* of mini-halos to their gas virial temperature, which is a function of the hosting halo mass and virialization redshift (e.g. Barkana & Loeb 2001):

$$T_{\text{vir}} = 1.98 \times 10^4 \left(\frac{\mu}{0.6}\right) \left(\frac{1+z}{10}\right) \left[\frac{M}{10^8 h^{-1} M_\odot}\right]^{2/3}, \quad (16)$$

where μ is the mean molecular weight respectively equal to $\mu = 1.22$ and 0.59 for neutral and fully ionized gas. Hence, according to the Λ CDM scenario, the smaller f_* the lower T_{vir} and the smaller the dark matter mass of the hosting halo. For example, by setting $f_*^{\text{Ly}\alpha\text{-cool}} = 0.1$ and a minimum virial temperature to form stars $T_{\text{vir}} = 2 \times 10^3$ K (e.g. Tegmark et al. 1997, Dijkstra et al. 2004), we obtain $f_* = (10^{-4}, 10^{-1})$, which is what we assumed in our model.

Fig. 21 (left) illustrates the tight relation between f_* and T_{vir} while showing the expected f_*/f_{dil} values for different f_* obtained by using eqs. 7-8. According to eq. 7, we have that f_{dil} is a function of f_* and $M_g = \Omega_b/\Omega_M M$, which can be also expressed in terms of f_* (and z) using eqs. 15-16. By varying f_* in our reference range we get that in most cases $f_{\text{dil}} \geq 1$. This means that, when f_* and M_g are tightly linked to each others, the amount of metals/gas ejected by PISN (or subsequent stellar generations) will always fill the entire

⁸ In more massive Ly α halos, we assume that PISN formed in each system have all the same mass, m_{PISN} .

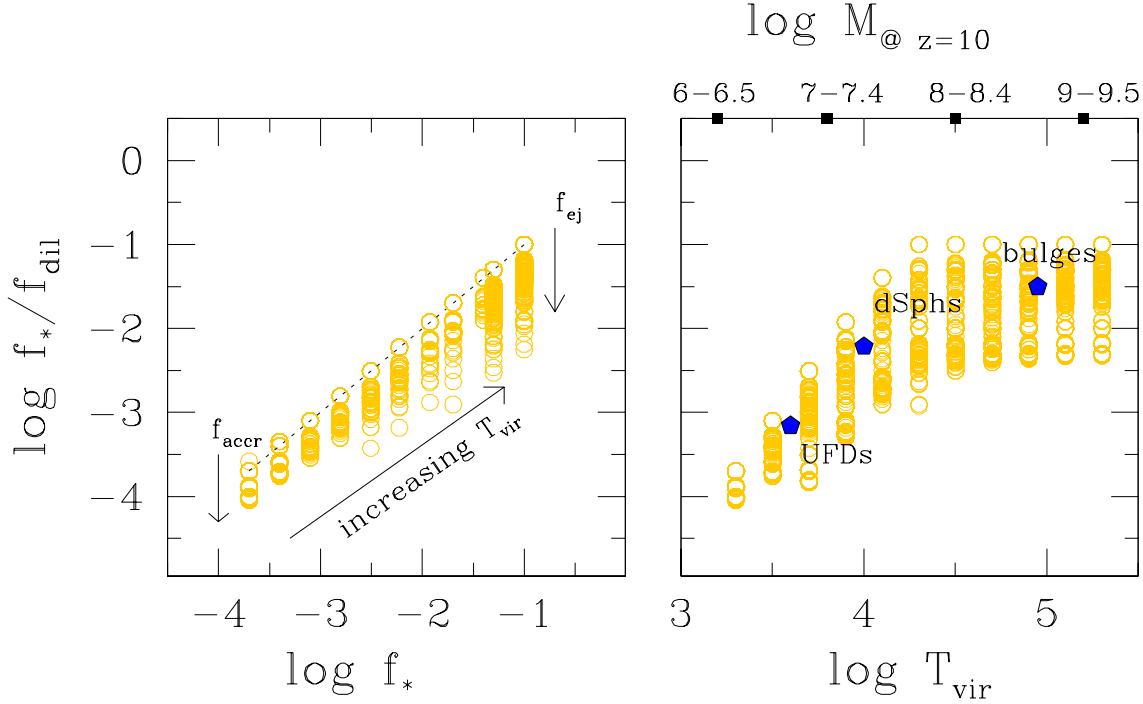


Figure 21. *Left:* Possible values of f_*/f_{dil} as a function of f_* (or T_{vir} , see text) and the other unknowns of the problem, f_{accr} and f_{ej} (open yellow circles). The black dotted line corresponds to the case $f_{\text{accr}} = 0$ and minimum f_{ej} . *Right:* f_*/f_{dil} as a function of T_{vir} and the corresponding halo virial mass evaluated at $z = 10$ (open yellow circles). The filled blue pentagones show the expected mean f_*/f_{dil} in environments with different T_{vir} or different dark matter halo masses.

galaxy and/or part of them will actually escape out of it. We thus need to use eq. 8.

To evaluate the ejected gas fraction in eq. 8, $f_{\text{ej}} = M_{\text{ej}}/M_{\text{g}}$, we can write M_{ej} as a function of the escape velocity of the galaxy, v_{e} , and of the SN explosion energy transformed in kinetic form, $1/2M_{\text{ej}}v_{\text{e}}^2 = E_{\text{kin}}$ (e.g. Larson 1974), where $E_{\text{kin}} = v_{\text{SN}}f_{\text{kin}} < E_{51} > M_{\text{g}}$ as discussed in Sec. 2.1. By assuming a Navarro-Frenk-White (NFW) prescription for the halo density profile, we can write the circular velocity at a position $x = r/r_{\text{vir}}$ with respect to the halo virial radius (Navarro et al. 1997). We get $v_{\text{e}}^2(x) = 2v_{\text{c}}^2[F(c_{\text{h}}x) + \frac{c_{\text{h}}x}{1+x}]/xF(c_{\text{h}})$ where $F(c_{\text{h}}) = \ln(1 + c_{\text{h}}) - (c_{\text{h}}/1 + c_{\text{h}})$ and c_{h} is the halo concentration parameter. The escape velocity from the centre ($x = 0$) of a NFW halo is $v_{\text{e}}^2 = 2[c_{\text{h}}/F(c_{\text{h}})]v_{\text{c}}^2$, where v_{c} is the circular velocity of the halo, which is again a function of T_{vir} and z (Barkana & Loeb 2001). In other words we have that $f_{\text{ej}} = f_{\text{ej}}(f_*, f_{\text{kin}}, z, c_{\text{h}})$, i.e. it also depends upon f_* and z .

By varying $f_* = (10^{-4} - 10^{-1})$, $z = (30 - 5)$, the concentration parameter $c_{\text{h}} = (1 - 30)$, $f_{\text{kin}} = (0.01 - 0.1)$, and $f_{\text{accr}} = (0.0 - 1.0)$ we get the results shown in Fig. 21 (left) for the mean PISN explosion energy (and mean stellar mass), $\langle E_{51} \rangle = 20$. It is clear from these calculations that $f_*/f_{\text{dil}} \in [10^{-4} - 10^{-1}]$ as assumed in our study. Furthermore, when f_* and f_{dil} are linked to each other via the Λ CDM cosmological model, we see that f_*/f_{dil} is mostly driven by f_* , i.e. the lower (higher) f_* , the lower (higher) f_*/f_{dil} .

We can use these findings to study f_*/f_{dil} as a function of T_{vir} and gain physical insights about the envi-

ronment of formation of massive first stars. This is illustrated in Fig. 21 (right), which also shows the correspondence⁹ between T_{vir} and M at $z = 10$. From this Figure we infer that $\langle f_*/f_{\text{dil}} \rangle \approx 0.0007$ in the smallest mini-haloes, $T_{\text{vir}} \approx 6 \times 10^3$, which are likely associated to ultra-faint dwarf galaxies (Salvadori & Ferrara 2009; Bovill & Ricotti 2009; Frebel et al. 2014; Wise et al. 2014; Bland-Hawthorn et al. 2015; Salvadori et al. 2015). More massive systems, which possibly become more luminous ‘‘classical’’ dwarf galaxies (e.g. Salvadori et al. 2015) have larger $\langle f_*/f_{\text{dil}} \rangle \approx 0.007$. Finally, we obtain that $\langle f_*/f_{\text{dil}} \rangle \approx 0.03$ in the most massive and rare haloes, $T_{\text{vir}} \approx 6 \times 10^4$, which likely associated to the bulges of galaxies that form via merging of high-sigma density peaks (e.g. Salvadori et al. 2010).

We recall that f_*/f_{dil} only determines the most likely $[\text{Fe}/\text{H}]$ range of PISN descendants (eq. 3) while $[\text{X}/\text{Fe}]$ is *not* a function of f_*/f_{dil} (eq. 4). To have an estimate of the typical $[\text{Fe}/\text{H}]$ for different f_*/f_{dil} we can use Fig. 2, since we know that the subsequent Pop II contribution does only alter the lowest $[\text{Fe}/\text{H}]$ -tail of the metallicity distribution function of PISN descendants Fig. 4. Hence, we infer that in classical dwarf spheroidal galaxies the PISN descendants can be most likely found at $[\text{Fe}/\text{H}] \approx -1.5$ while in the bulges of more massive systems at $[\text{Fe}/\text{H}] \approx -0.5$. Interestingly, these values are similar to the $[\text{Fe}/\text{H}]$ range of sub-solar $[\text{Zn}/\text{Fe}]$ measurements respectively reported in the classical dwarf

⁹ The two values of M refer to different choices of the mean molecular weight μ , see eq. 16.

galaxy Sculptor and in the Milky Way bulge (see references in Skuladottir et al. 2018 and their Fig. 4 for a complete view of $[\text{Zn}/\text{Fe}]$ across different environments).

If the stellar halos of galaxies are the result of accreting satellites with different masses, then the corresponding f_*/f_{dil} might span a very wide range of values (Fig.2). As a consequence, to catch the PISN descendants in these environments we should look for stars around the most likely $[\text{Fe}/\text{H}]$ range among *all* different models, i.e. $-2.5 < [\text{Fe}/\text{H}] < -1.5$ (Fig.7), as discussed in our observational strategy (Sec. 6.2.2).

8 CONCLUSIONS

We presented a novel method to determine the key element ratios we should look for to identify the chemical signature of very massive first stars exploding as PISN. Independent on the unknowns related to early cosmic star-formation, metal diffusion and mixing, when the mass fraction of heavy elements from PISN represents $\geq 50\%$ of the total, our parametric study shows that there is always an under-abundance of the key element ratios $[(\text{N}, \text{Cu}, \text{Zn})/\text{Fe}] < 0$. In fact, N, Cu, and Zn are so scarcely produced by PISN that even when subsequent generations of Pop II stars do contribute to the enrichment their under-abundance with respect to Fe is preserved. Note that if primordial PISN were fast rotators the (under-)production of Cu and Zn would have not been altered, while the internal mixing might have induced efficient N production (Takahashi et al. 2018). Furthermore, due to the activation of the CNO cycle, the N abundance can largely increase in bright Red Giant Branch (RGB) stars. With current telescopes, RGB stars represent the majority of stellar targets for high-resolution spectroscopic follow-up in nearby dwarf galaxies. In conclusion, we can assert that the descendants of PISN, i.e. long-lived stars born in a PISN-imprinted ISM, should have $[(\text{Cu}, \text{Zn})/\text{Fe}] < 0$.

Our model results also show that PISN descendants can cover a broad $[\text{Fe}/\text{H}]$ range across the overall parameter space but on average they most likely appear at $[\text{Fe}/\text{H}] \approx -2$. These findings nicely agree with previous studies that employed a completely different (cosmological) approach (Salvadori et al. 2007; Karlsson et al. 2008; de Bannassuti et al. 2017), thus strengthening our method and approximations. At these high $[\text{Fe}/\text{H}]$, SNIa might have also played a role in the chemical evolution. Yet, in our work we demonstrated that an ISM polluted by Pop II and SNIa typically have larger $[(\text{Cu}, \text{Zn})/\text{Fe}]$ ratio than ISM also imprinted by PISN. Furthermore, the chemical abundance patterns are quite different, thus allowing us to check and account for possible degeneracies.

Among literature stars at $[\text{Fe}/\text{H}] \approx -2$ we pinpointed BD +80° 245 that has sub-solar $[(\text{Cu}, \text{Zn})/\text{Fe}]$. Our re-analysis of the new and available spectra for BD +80° 245, including NLTE corrections for Cu, demonstrate that this star might be a convincing example of a PISN descendants. In fact, the three killing element ratios are sub-solar and its (almost) complete chemical abundance pattern agrees with our model results for $f_*/f_{\text{dil}} = 10^{-3}$ and an ISM equally polluted by PISN and normal Pop II stars with $m_{\text{popII}} > 8M_{\odot}$. These core-collapse SN typically evolve on a ≈ 30 Myr timescale, which implies that there is likely a delay between Pop III

and the subsequent star-formation, in agreement with cosmological simulations of the first star-forming galaxies (e.g. Bromm et al. 2003; Wise et al. 2014; Jeon et al. 2014). This positive finding suggests that to search for the rare PISN descendants by performing Zn surveys with the HERMES and WEAVE spectrographs is not only feasible but extremely promising.

It is interesting to note that Hartwig et al. 2019, although not investigating the imprint by PISN, found that N, Cu, and Zn are some of the most important elements to discriminate $[\text{Fe}/\text{H}] < -3$ stars that are enriched by a single (mono) or multiple first stars with masses $\leq 140M_{\odot}$. The concordance of these findings by two independent studies aimed at addressing very different questions related to primordial stars, strengthen the observational need for additional measurements of these key chemical elements.

Our parametric study is extremely general and can therefore be applied to different “systems” that retain the chemical signature of PISN. Not only present-day stars dwelling in different environments (dwarf galaxies, stellar halos, bulges) but also high-redshift gas in/and around galaxies that can be observed as Damped Ly α systems along with the Circum- and Inter- Galactic Medium (CGM, IGM). Cosmological simulations of metal-enrichment from the first galaxies have shown that very massive first stars exploding as PISN produce much larger metal-enriched bubbles than their lower mass companions, and the differences in the IGM morphology are quite remarkable even at $z \approx 4$ (Pallottini et al. 2014). Looking for the lack of our key elements in the CGM of high- z galaxies can thus be a complementary way to probe the existence of PISN and to understand their persistence across cosmic times (e.g. Mebane et al. 2017). As for the case of BD +80° 245, once identified a system that lacks our killing element ratios, high resolution spectroscopic follow-up (e.g. with HIRES on ELT) can fully characterise its abundance pattern. Our work showed that statistical comparison between the observed patterns and those predicted by our models is able to reveal the most likely mass of the Pop III/II pollutants (Sec. 5.2) and their environment of formation (Sec. 7).

We should conclude by mentioning that several studies have recently focused on the key chemical abundance ratios of “second-generation” stars, i.e. stars formed out from an environment solely imprinted by the first stars (e.g. Hartwig et al. 2018 and Takahashi et al. 2018b for the PISN). Although our results for the “direct descendants” of PISN, i.e. for an ISM imprinted by PISN at 100% level, are consistent with these works, we should underline that our simple *parametric approach* is completely different in both methods and aim. Our goal was in fact to develop new strategy to identify *all descendants* of very massive first stars. These stars, in fact, are clearly more common than second-generation stars solely imprinted by PISN. Furthermore, once interpreted with cosmological chemical evolution models for the Local Group formation, they can provide key information on both the first stars properties and early cosmic star-formation (Salvadori et al. 2015; de Bannassuti et al. 2017). By building-up a sample of PISN descendants, therefore, we can not only probe the existence of very massive first stars but also provide tight empirical constrain on their unknown initial mass function.

ACKNOWLEDGEMENTS

We thank the anonymous referee for his/her careful reading of the paper and for his/her very positive, constructive, and deep comments. SS warmly thank Andrea Ferrara for the incisive expression “killing elements” and acknowledges the Italian Ministry for Education, University, and Research through a Levi Montalcini Fellowship. This project has received funding from the European Research Council (ERC) under the European Union’s Horizon 2020 research and innovation programme (grant agreement No 804240). Á.S. acknowledges funds from the Alexander von Humboldt Foundation in the framework of the Sofja Kovalevskaja Award endowed by the Federal Ministry of Education and Research. We are grateful at the Programme National de Cosmologie et Galaxies of CNRS that granted us observation time with SOPHIE, under programme 17B.PNCG.BONI. This research has made use of the Keck Observatory Archive (KOA), which is operated by the W. M. Keck Observatory and the NASA Exoplanet Science Institute (NExScI), under contract with the National Aeronautics and Space Administration. The Keck-HIRES observations were acquired during program G401H, PI Meléndez.

REFERENCES

- Abel T., Bryan G. L., Norman M. L., 2002, *Science*, 295, 93
- Aguado D. S., González Hernández J. I., Allende Prieto C., Rebolo R., 2017, *aap*, 605, A40
- Allende Prieto C. et al., 2014, *aap*, 568, A7
- Andersen T., Soerensen G., 1973, *J. Quant. Spectr. Rad. Transf.*, 13, 369
- Andrievsky S., Bonifacio P., Caffau E., Korotin S., Spite M., Spite F., Sbordone L., Zhukova A. V., 2018, *MNRAS*, 473, 3377
- Aoki W., Tominaga N., Beers T. C., Honda S., Lee Y. S., 2014, *Science*, 345, 912
- Arenou F. et al., 2018, *ArXiv e-prints*
- Barbuy B. et al., 2015, *A&A*, 580, A40
- Barden S. C. et al., 2010, in *procspie*, Vol. 7735, Ground-based and Airborne Instrumentation for Astronomy III, p. 773509
- Barkana R., Loeb A., 2001, *Physics reports*, 349, 125
- Beers T. C., Christlieb N., 2005, *ARA&A*, 43, 531
- Benítez-Llambay A., Navarro J. F., Abadi M. G., Gottlöber S., Yepes G., Hoffman Y., Steinmetz M., 2015, *MNRAS*, 450, 4207
- Bigelow B. C., Dressler A. M., Shectman S. A., Epps H. W., 1998, in *procspie*, Vol. 3355, Optical Astronomical Instrumentation, D’Odorico S., ed., pp. 225–231
- Bland-Hawthorn J., Sutherland R., Webster D., 2015, *ApJ*, 807, 154
- Bonifacio P. et al., 2011, *Astronomische Nachrichten*, 332, 251
- Bonifacio P., Caffau E., Ludwig H.-G., 2010, *aap*, 524, A96
- Bonifacio P., Caffau E., Ludwig H.-G., Spite M., Plez B., Steffen M., Spite F., 2013, *Memorie della Società Astronomica Italiana Supplementi*, 24, 138
- Bonifacio P. et al., 2018a, *aap*, 611, A68
- Bonifacio P. et al., 2015, *A&A*, 579, A28
- Bonifacio P. et al., 2018b, *A&A*, in press
- Bonifacio P., Limongi M., Chieffi A., 2003, *Nature*, 422, 834
- Bouchy F., Sophie Team, 2006, in *Tenth Anniversary of 51 Peg-b: Status of and prospects for hot Jupiter studies*, Arnold L., Bouchy F., Moutou C., eds., pp. 319–325
- Bovill M. S., Ricotti M., 2009, *ApJ*, 693, 1859
- Bressan A., Marigo P., Girardi L., Salasnich B., Dal Cero C., Rubele S., Nanni A., 2012, *MNRAS*, 427, 127
- Bromm V., 2013, *Reports on Progress in Physics*, 76, 112901
- Bromm V., Ferrara A., Coppi P. S., Larson R. B., 2001, *MNRAS*, 328, 969
- Bromm V., Yoshida N., Hernquist L., 2003, *ApJL*, 596, L135
- Bromm V., Yoshida N., Hernquist L., McKee C. F., 2009, *Nature*, 459, 49
- Brook C. B., Kawata D., Scannapieco E., Martel H., Gibson B. K., 2007, *ApJ*, 661, 10
- Buder S. et al., 2018, *ArXiv e-prints*
- Caffau E. et al., 2013, *aap*, 560, A15
- Caffau E., Gallagher A. J., Bonifacio P., Spite M., Duffau S., Spite F., Monaco L., Sbordone L., 2018, *A&A*, in press
- Caffau E., Ludwig H.-G., Steffen M., Freytag B., Bonifacio P., 2011, *solphys*, 268, 255
- Carney B. W., Wright J. S., Sneden C., Laird J. B., Aguilar L. A., Latham D. W., 1997, *aj*, 114, 363
- Castelli F., Kurucz R. L., 2003, in *Modelling of Stellar Atmospheres*, Proceedings of the 210th Symposium of the International Astronomical Union, pp. P20, [astro-ph/0405087](https://arxiv.org/abs/astro-ph/0405087)
- Cayrel R. et al., 2004, *A&A*, 416, 1117
- Chiaki G., Susa H., Hirano S., 2018, *mnras*, 475, 4378
- Collet R., Nordlund Å., Asplund M., Hayek W., Trampedach R., 2018, *mnras*, 475, 3369
- Cooke R. J., Madau P., 2014, *ApJ*, 791, 116
- Dalton G. et al., 2016, in *procspie*, Vol. 9908, Ground-based and Airborne Instrumentation for Astronomy VI, p. 99081G
- de Bannassuti M., Salvadori S., Schneider R., Valiante R., Omukai K., 2017, *MNRAS*, 465, 926
- de Jong R. S. et al., 2016, in *procspie*, Vol. 9908, Ground-based and Airborne Instrumentation for Astronomy VI, p. 99081O
- De Silva G. M. et al., 2015, *mnras*, 449, 2604
- Dekker H., D’Odorico S., Kaufer A., Delabre B., Kotzlowski H., 2000, in *procspie*, Vol. 4008, Optical and IR Telescope Instrumentation and Detectors, Iye M., Moorwood A. F., eds., pp. 534–545
- Duffau S. et al., 2017, *aap*, 604, A128
- Fernández-Trincado J. G., 2019, *ApJS*, in prep.
- Frebel A., Bromm V., 2012, *ApJ*, 759, 115
- Frebel A., Simon J. D., Kirby E. N., 2014, *ApJ*, 786, 74
- Fulbright J. P., 2000, *aj*, 120, 1841
- Gaia Collaboration, Brown A. G. A., Vallenari A., Prusti T., de Bruijne J. H. J., Babusiaux C., Bailer-Jones C. A. L., 2018, *ArXiv e-prints*
- Gaia Collaboration et al., 2016, *aap*, 595, A1
- Gallagher A. J., Caffau E., Bonifacio P., Ludwig H.-G., Steffen M., Homeier D., Plez B., 2017, *aap*, 598, L10
- Gillis J. R., Goldman A., Stark G., Rinsland C. P., 2001, *jqsr*, 68, 225
- Goldman A., Gillis J. R., 1981, *jqsr*, 25, 111
- González Hernández J. I., Bonifacio P., Ludwig H.-G., Caffau E., Behara N. T., Freytag B., 2010, *aap*, 519, A46
- Greif T. H., 2015, *Computational Astrophysics and Cosmology*, 2
- Greif T. H., Bromm V., Clark P. C., Glover S. C. O., Smith R. J., Klessen R. S., Yoshida N., Springel V., 2012, *MNRAS*, 424, 399
- Greif T. H., Glover S. C. O., Bromm V., Klessen R. S., 2009, *MNRAS*, 392, 1381
- Greif T. H., Johnson J. L., Bromm V., Klessen R. S., 2007, *ApJ*, 670, 1
- Hartwig T. et al., 2018, *mnras*, 478, 1795
- Heger A., Woosley S. E., 2002, *ApJ*, 567, 532
- Heiter U. et al., 2015, *physscr*, 90, 054010
- Hirano S., Hosokawa T., Yoshida N., Omukai K., Yorke H. W., 2015, *MNRAS*, 448, 568
- Hirano S., Hosokawa T., Yoshida N., Umeda H., Omukai K., Chiaki G., Yorke H. W., 2014, *ApJ*, 781, 60
- Hosokawa T., Omukai K., Yoshida N., Yorke H. W., 2011, *Science*, 334, 1250

- Ivans I. I., Sneden C., James C. R., Preston G. W., Fulbright J. P., Höflich P. A., Carney B. W., Wheeler J. C., 2003, *apj*, 592, 906
- Iwamoto K., Brachwitz F., Nomoto K., Kishimoto N., Umeda H., Hix W. R., Thielemann F.-K., 1999, *ApJS*, 125, 439
- Iwamoto N., Umeda H., Tominaga N., Nomoto K., Maeda K., 2005, *Science*, 309, 451
- Jeon M., Pawlik A. H., Bromm V., Milosavljević M., 2014, *MNRAS*, 444, 3288
- Karlsson T., Johnson J. L., Bromm V., 2008, *ApJ*, 679, 6
- Keller S. C. et al., 2014, *Nature*, 506, 463
- Keller S. C. et al., 2007, *pasa*, 24, 1
- Kobayashi C., Umeda H., Nomoto K., Tominaga N., Ohkubo T., 2006, *ApJ*, 653, 1145
- Kock M., Richter J., 1968, *Zeitschrift für Astrophysik*, 69, 180
- Korotin S. A., Andrievsky S. M., Zhukova A. V., 2018, *MNRAS*, 480, 965
- Kurucz R. L., 2005, *Memorie della Societa Astronomica Italiana Supplementi*, 8, 14
- Latham D. W., Stefanik R. P., Torres G., Davis R. J., Mazeh T., Carney B. W., Laird J. B., Morse J. A., 2002, *aj*, 124, 1144
- Lodders K., Palme H., Gail H.-P., 2009, *Landolt Börnstein*
- Madau P., Ferrara A., Rees M. J., 2001, *ApJ*, 555, 92
- Mannucci F., Della Valle M., Panagia N., 2006, *MNRAS*, 370, 773
- Mashonkina L. I., Sitnova T. N., Pakhomov Y. V., 2016, *Astronomy Letters*, 42, 606
- McKee C. F., Tan J. C., 2008, *ApJ*, 681, 771
- Meynet G., Maeder A., 2002, *A&A*, 390, 561
- Navarro J. F., Frenk C. S., White S. D. M., 1997, *ApJ*, 490, 493
- Noguchi K. et al., 2002, *pasj*, 54, 855
- Oñorbe J., Boylan-Kolchin M., Bullock J. S., Hopkins P. F., Kereš D., Faucher-Giguère C.-A., Quataert E., Murray N., 2015, *MNRAS*, 454, 2092
- Omukai K., 2012, *pasj*, 64
- Pallottini A., Ferrara A., Bovino S., Vallini L., Gallerani S., Maiolino R., Salvadori S., 2017, *MNRAS*, 471, 4128
- Pallottini A., Ferrara A., Gallerani S., Salvadori S., D’Odorico V., 2014, *MNRAS*, 440, 2498
- Raiteri C. M., Villata M., Navarro J. F., 1996, *A&A*, 315, 105
- Robin A. C., Reylé C., Derrière S., Picaud S., 2003, *aap*, 409, 523
- Roederer I. U., Barklem P. S., 2018, *apj*, 857, 2
- Roederer I. U., Preston G. W., Thompson I. B., Shtetman S. A., Sneden C., Burley G. S., Kelson D. D., 2014, *aj*, 147, 136
- Rogers K. et al., 2014, in *procspie*, Vol. 9147, *Ground-based and Airborne Instrumentation for Astronomy V*, p. 91476H
- Rossi S., Beers T. C., Sneden C., Sevastyanenko T., Rhee J., Marsteller B., 2005, *aj*, 130, 2804
- Salvadori S., Ferrara A., 2009, *MNRAS*, 395, L6
- Salvadori S., Ferrara A., Schneider R., 2008, *MNRAS*, 386, 348
- Salvadori S., Ferrara A., Schneider R., Scannapieco E., Kawata D., 2010, *MNRAS*, 401, L5
- Salvadori S., Schneider R., Ferrara A., 2007, *MNRAS*, 381, 647
- Salvadori S., Skúladóttir Á., Tolstoy E., 2015, *MNRAS*, 454, 1320
- Salvadori S., Tolstoy E., Ferrara A., Zaroubi S., 2014, *MNRAS*, 437, L26
- Sbordone L., Bonifacio P., Castelli F., Kurucz R. L., 2004, *Memorie della Societa Astronomica Italiana Supplementi*, 5, 93
- Sbordone L., Caffau E., Bonifacio P., Duffau S., 2014, *aap*, 564, A109
- Schaerer D., 2002, *A&A*, 382, 28
- Schneider R., Ferrara A., Natarajan P., Omukai K., 2002, *ApJ*, 571, 30
- Schneider et al., 2004, *MNRAS*, 351, 1379
- Sharma S., Bland-Hawthorn J., Johnston K. V., Binney J., 2011, *apj*, 730, 3
- Sheinin A. et al., 2014, in *procspie*, Vol. 9147, *Ground-based and Airborne Instrumentation for Astronomy V*, p. 91470Y
- Silk J., 1977, *ApJ*, 214, 718
- Skúladóttir Á., Salvadori S., Pettini M., Tolstoy E., Hill V., 2018, *A&A*, 615, A137
- Skúladóttir Á., Tolstoy E., Salvadori S., Hill V., Pettini M., 2017, *A&A*, 606, A71
- Smith B. D., Wise J. H., O’Shea B. W., Norman M. L., Khochfar S., 2015, *MNRAS*, 452, 2822
- Spite M., Caffau E., Bonifacio P., Spite F., Ludwig H.-G., Plez B., Christlieb N., 2013, *A&A*, 552, A107
- Spite M., Spite F., François P., Bonifacio P., Caffau E., Salvadori S., 2018, *aap*, 617, A56
- Stark G., Brault J. W., Abrams M. C., 1994, *Journal of the Optical Society of America B Optical Physics*, 11, 3
- Starkenburger E. et al., 2017, *mnras*, 471, 2587
- Susa H., Hasegawa K., Tominaga N., 2014, *apj*, 792, 32
- Sutin B. M., McWilliam A., 2003, in *procspie*, Vol. 4841, *Instrument Design and Performance for Optical/Infrared Ground-based Telescopes*, Iye M., Moorwood A. F. M., eds., pp. 1357–1366
- Takeda Y., Hashimoto O., Taguchi H., Yoshioka K., Takada-Hidai M., Saito Y., Honda S., 2005, *pasj*, 57, 751
- Taylor K., Cannon R. D., Watson F. G., 1997, in *procspie*, Vol. 2871, *Optical Telescopes of Today and Tomorrow*, Ardeberg A. L., ed., pp. 145–149
- Tolstoy E., Hill V., Tosi M., 2009, *ARA&A*, 47, 371
- Tumlinson J., 2006, *ApJ*, 641, 1
- Tumlinson J., 2010, *ApJ*, 708, 1398
- Vernet J. et al., 2011, *aap*, 536, A105
- Vogt S. S. et al., 1994, in *procspie*, Vol. 2198, *Instrumentation in Astronomy VIII*, Crawford D. L., Craine E. R., eds., p. 362
- Volonteri M., 2010, *A&A Rev.*, 18, 279
- Warner B., 1968, *MNRAS*, 140, 53
- White S. D. M., Springel V., 2000, in *The First Stars*, Weiss A., Abel T. G., Hill V., eds., p. 327
- Wise J. H., Demchenko V. G., Halicek M. T., Norman M. L., Turk M. J., Abel T., Smith B. D., 2014, *MNRAS*, 442, 2560
- Wise J. H., Turk M. J., Norman M. L., Abel T., 2012, *ApJ*, 745, 50
- Woosley S. E., Weaver T. A., 1995, *ApJS*, 101, 181
- Yong D. et al., 2013, *ApJ*, 762, 27

9 APPENDIX A

In this Appendix we present the results our χ^2 analysis to determine the best-fitting model of BD +80° 245 across the whole range of model free parameters. These findings are reported in Fig. 22, where χ^2_ν is shown as a function of m_{PISN} (x-axis) f_*/f_{dil} (different rows), f_{PISN} (different columns), and t_{popII} (different colours). We see that for $f_{\text{PISN}} = 0.9$ (left column) only $m_{\text{PISN}} \approx 200M_\odot$ models give a relatively good fit of BD +80° 245, i.e. $\chi^2_\nu < 2$, a result that is almost independent on t_{popII} . We can understand why this is the case by looking at the left panel of Fig. 4 where we see that $[\text{Fe}/\text{H}]_{\text{ISM}} \approx -2$ only for $m_{\text{PISN}} \approx 200M_\odot$, and independent of t_{popII} . In the right panel of Fig. 4, for $f_{\text{PISN}} = 0.5$, we see that all models with $m_{\text{PISN}} \leq 200M_\odot$ and $t_{\text{popII}} > 20 \text{ Myr}$ give $[\text{Fe}/\text{H}]_{\text{ISM}} \approx -2$. This is because the iron-pollution of the ISM is mainly driven by normal core-collapse SNe, which provide enough iron to reach the observed value only if $> 20 \text{ Myr}$ (see Fig. 5). For these reasons, Fig. 22 shows that the larger the contribution from Pop II stars, the higher the number of models with $t_{\text{popII}} = 30 \text{ Myr}$ (black points) that provide $\chi^2_\nu < 2$. In particular, we find that for $f_{\text{PISN}} = 0.5$ and $f_*/f_{\text{dil}} = 10^{-4}$ (right-most and lower-most panel) all models with $t_{\text{popII}} = 30 \text{ Myr}$ give $\chi^2_\nu < 2$. These are our best-

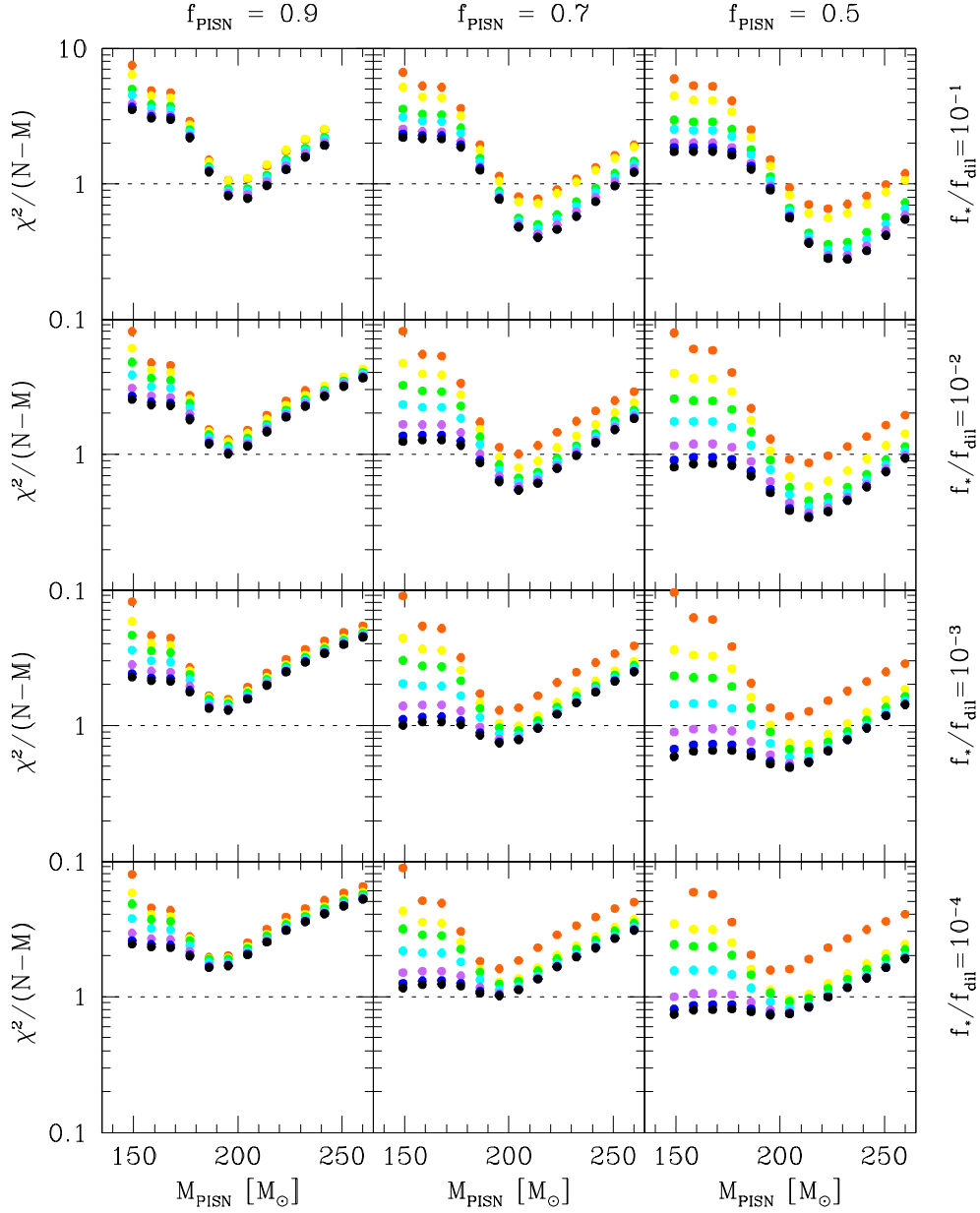


Figure 22. The χ^2 distribution normalized to the degree of freedom as a function of the PISN mass and for different combinations of the other free parameters. The panels illustrate how the results change with f_{PISN} (*columns*) and f_*/f_{dust} (*rows*), while different colours in each panel show the time passed since the Pop II formation, from *red* ($t_{\text{popII}} \approx 3$ Myr, uppermost symbols) to *black* ($t_{\text{popII}} \approx 30$ Myr, lower-most symbols).

fitting models shown in Fig. 20. Following Ishigaki et al. (2019) we checked that for all of them the probability of the χ^2 distribution for $(N - M)$ degrees of freedom between $x^2 = \chi^2$ and infinity provide the largest values. Among all these best-fitting models, we find that the one that reproduces the abundance pattern of BD +80° 245 at best corresponds to $m_{\text{PISN}} \leq 223 M_{\odot}$, which gives $\chi^2_{\nu} = 0.99$.

10 APPENDIX B

In this Appendix we provide all the tables that illustrate what all the lines used to determine the different chemical elements reported in Table 1.

Table 2. OH lines used for the determination of the oxygen abundance.

λ nm	log gf	J_{low}	J_{up}	E_{low} cm ⁻¹
307.43704	-2.581	3.5	4.5	429.458
308.12544	-1.902	17.5	18.5	6148.942
308.32790	-2.066	4.5	4.5	355.900
308.33753	-2.804	4.5	3.5	355.900
308.48950	-1.894	18.5	19.5	6801.926
308.51993	-1.973	5.5	5.5	544.809
308.53170	-2.865	5.5	4.5	544.809
308.62241	-1.888	20.5	21.5	7459.105
308.63920	-2.305	2.5	1.5	83.719
308.90082	-1.887	19.5	20.5	7483.875
308.97356	-1.837	7.5	7.5	1029.092
308.97748	-3.101	2.5	3.5	288.769
308.98130	-3.191	1.5	2.5	187.491
308.98501	-2.328	2.5	2.5	288.769
308.98669	-2.545	1.5	1.5	187.491
308.98958	-2.972	7.5	6.5	1029.092
309.02717	-3.077	3.5	4.5	429.275
309.03683	-2.174	3.5	3.5	429.275
309.04537	-3.462	0.5	1.5	126.291
309.04861	-2.859	0.5	0.5	126.291
309.23976	-1.786	8.5	8.5	1324.291
310.12308	-2.127	5.5	4.5	543.575
310.32691	-2.798	3.5	3.5	429.458
310.33452	-2.354	3.5	2.5	429.458
310.60199	-1.645	12.5	12.5	2852.485
310.65461	-2.076	6.5	5.5	767.458
310.74582	-2.824	4.5	4.5	608.188
310.75561	-2.257	4.5	3.5	608.188
311.30780	-3.274	3.5	2.5	429.275
311.33656	-1.644	12.5	12.5	3348.880
311.47735	-1.601	14.5	14.5	3819.156
312.39487	-1.960	9.5	8.5	1650.790
312.76877	-1.584	15.5	15.5	4939.902
313.91699	-1.559	17.5	17.5	6157.854
314.07350	-1.950	10.5	9.5	2450.279
315.10035	-1.863	13.5	12.5	3311.982
316.71693	-1.541	21.5	21.5	8944.563
317.44843	-1.821	16.5	15.5	4904.629
317.53019	-1.543	22.5	22.5	9709.602
319.48479	-1.821	17.5	16.5	6148.942
320.09601	-1.800	19.5	18.5	6776.431
325.25948	-1.809	24.5	23.5	10462.394
325.54929	-1.809	23.5	22.5	10484.962

Table 3. Atomic data for the lines of CuI.

λ nm	log gf hfs	log gf line
324.7511	-1.379	-0.05
324.7513	-1.028	
324.7515	-1.379	
324.7517	-0.957	
324.7520	-1.426	
324.7555	-0.288	
324.7558	-1.567	
327.3927	-1.375	-0.35
327.3929	-1.024	
327.3931	-2.074	
327.3933	-1.723	
327.3971	-1.024	
327.3972	-1.375	
327.3975	-1.024	
327.3976	-1.375	
510.5504	-3.720	-1.51
510.5513	-2.766	
510.5516	-2.813	
510.5517	-3.090	
510.5521	-2.720	
510.5526	-2.398	
510.5536	-2.051	
510.5563	-1.942	

The gf values are from Warner (1968).

Table 4. Atomic data for the lines of ZnI.

λ nm	log gf	J_{low}	J_{up}	E_{low} cm ⁻¹	Ref.
330.2584	-0.057	1.0	2.0	32501.421	1
330.2941	-0.534	1.0	1.0	32501.421	1
481.0528	-0.137	2.0	1.0	32890.352	2

References for gf values:

- 1 : Andersen & Soerensen (1973)
- 2 : Kock & Richter (1968)

Table 5. Atomic data used to synthesize the NH 336 nm band: Ca to Ni.

λ nm	$\log gf$	J_{low}	J_{up}	E_{low} cm ⁻¹
Ca I				
336.1912	-0.580	3.0	2.0	45052.375
336.2133	-1.260	2.0	2.0	45050.418
336.2286	-2.520	1.0	2.0	45049.074
Ti I				
335.8271	-1.190	2.0	2.0	0.000
335.8479	+0.370	5.0	4.0	48461.965
336.0989	-1.230	3.0	3.0	170.134
336.1266	-1.080	3.0	3.0	170.134
336.1831	-1.460	3.0	2.0	170.134
Ti II				
336.0170	-1.614	0.5	1.5	9850.900
336.1060	-2.171	1.5	0.5	9930.690
336.1218	+0.280	3.5	4.5	225.730
V II				
336.1496	-1.200	4.0	5.0	19112.930
Cr I				
336.2216	-0.513	6.0	5.0	20519.553
336.2354	-1.025	2.0	2.0	24299.844
Cr II				
335.8491	-1.384	2.5	1.5	19797.881
336.0291	+0.250	3.5	3.5	25033.699
336.1767	-0.926	2.5	3.5	25046.760
Fe I				
335.7568	-1.959	3.0	3.0	58831.227
335.8635	-2.170	3.0	3.0	57160.137
335.9118	-2.582	4.0	3.0	57155.852
335.9404	-2.221	1.0	2.0	24772.016
335.9486	-3.730	5.0	4.0	6928.268
335.9808	-1.761	4.0	5.0	26627.607
336.0926	-2.383	1.0	1.0	19552.477
336.0973	-3.895	2.0	3.0	18378.186
336.1566	-3.059	3.0	4.0	20874.480
336.1950	-1.243	1.0	2.0	22946.814
Fe II				
335.7927	-2.754	3.5	2.5	33501.254
335.8247	-2.484	2.5	3.5	31387.947
335.8779	-4.221	2.5	2.5	13474.411
336.0115	-2.670	5.5	5.5	32909.906
Co II				
335.8599	-2.341	3.0	2.0	17771.711
Ni I				
335.9101	+0.019	5.0	4.0	57829.406
336.1237	-0.282	4.0	4.0	57810.492
336.1551	-1.390	2.0	2.0	879.813

Table 6. Atomic data used to synthesize the NH 336 nm band: Y to Er.

λ nm	$\log gf$	J_{low}	J_{up}	E_{low} cm ⁻¹
Y II				
336.1986	-0.230	2.0	1.0	14832.854
Zr II				
335.9955	-0.260	4.5	4.5	11984.460
Ce II				
336.0532	+0.535	7.5	7.5	11309.972
336.1763	-0.432	6.5	6.5	3793.634
Nd II				
335.9766	-0.260	8.5	7.5	5085.640
Gd II				
335.8432	-0.660	3.5	3.5	3444.235
335.8625	+0.152	3.5	4.5	261.841
336.0712	-0.591	3.5	3.5	261.841
336.2239	+0.294	4.5	5.5	633.273
Dy II				
335.8602	-1.359	8.5	8.5	0.000
335.9462	+0.567	8.5	7.5	14895.060
Er II				
335.8153	-0.631	4.5	3.5	5132.608

Table 7. Atomic data and hyperfine structure for ScII and CoI used in the synthesis of the NH band

λ nm	$\log gf$	$\log(hfs)$	J_{low}	J_{up}	E_{low} cm ⁻¹
ScII					
	-0.770				
335.9675		-0.626	2.0	2.0	67.720
335.9675		-1.196	2.0	2.0	67.720
335.9677		-1.024	2.0	2.0	67.720
335.9677		-1.038	2.0	2.0	67.720
335.9677		-1.196	2.0	2.0	67.720
335.9679		-1.038	2.0	2.0	67.720
335.9679		-1.049	2.0	2.0	67.720
335.9679		-1.720	2.0	2.0	67.720
335.9680		-1.049	2.0	2.0	67.720
335.9680		-1.222	2.0	2.0	67.720
335.9680		-3.146	2.0	2.0	67.720
335.9681		-1.222	2.0	2.0	67.720
335.9681		-1.398	2.0	2.0	67.720
	-0.790				
336.1261		-0.594	1.0	1.0	0.000
336.1261		-0.790	1.0	1.0	0.000
336.1266		-0.790	1.0	1.0	0.000
336.1266		-0.794	1.0	1.0	0.000
336.1266		-1.975	1.0	1.0	0.000
336.1269		-0.794	1.0	1.0	0.000
336.1269		-1.049	1.0	1.0	0.000
336.1931	-0.630		1.0	0.0	0.00
CoI					
	0.127				
336.1487		-1.426	5.5	4.5	54367.430
336.1494		-1.308	5.5	4.5	54367.430
336.1494		-1.878	5.5	4.5	54367.430
336.1503		-1.190	5.5	4.5	54367.430
336.1503		-1.667	5.5	4.5	54367.430
336.1503		-2.878	5.5	4.5	54367.430
336.1516		-1.078	5.5	4.5	54367.430
336.1516		-1.571	5.5	4.5	54367.430
336.1516		-2.671	5.5	4.5	54367.430
336.1533		-0.974	5.5	4.5	54367.430
336.1533		-1.535	5.5	4.5	54367.430
336.1533		-2.643	5.5	4.5	54367.430
336.1552		-0.878	5.5	4.5	54367.430
336.1552		-1.551	5.5	4.5	54367.430
336.1552		-2.723	5.5	4.5	54367.430
336.1575		-0.788	5.5	4.5	54367.430
336.1575		-1.633	5.5	4.5	54367.430
336.1575		-2.915	5.5	4.5	54367.430
336.1601		-0.704	5.5	4.5	54367.430
336.1601		-1.851	5.5	4.5	54367.430
336.1601		-3.304	5.5	4.5	54367.430

Table 8. Molecular data of CH and OH used to synthesise the NH 336 nm band.

λ nm	$\log gf$	J_{low}	J_{up}	E_{low} cm ⁻¹
CH				
336.1977	-0.682	36.5	37.5	21250.174
336.1837	-0.670	37.5	38.5	21249.012
OH				
335.9900	-1.401	32.5	31.5	17591.371
335.9790	-2.226	18.5	18.5	16241.062
336.0598	-1.686	27.5	26.5	16029.838
336.0075	-2.094	20.5	19.5	14532.071
336.0417	-2.656	13.5	12.5	13621.247

Table 9. Molecular data of NH used to synthesise the NH 336 nm band (first part).

λ nm	$\log gf$	J_{low}	J_{up}	E_{low} cm ⁻¹
335.7557	-1.918	0.0	1.0	31.574
335.7662	-2.056	2.0	1.0	32.506
335.7736	-1.302	3.0	3.0	326.030
335.7835	-2.159	4.0	3.0	326.909
335.8050	-1.171	4.0	4.0	488.704
335.8053	-1.590	1.0	2.0	0.000
335.8135	-2.221	5.0	4.0	489.460
335.8292	-2.015	1.0	2.0	97.567
335.8300	-1.072	5.0	5.0	683.546
335.8309	-1.995	3.0	2.0	97.718
335.8404	-1.665	2.0	3.0	3220.365
335.8417	-1.720	2.0	2.0	98.676
335.8503	-0.992	6.0	6.0	910.056
335.8665	-2.042	4.0	3.0	195.513
335.8678	-2.087	2.0	3.0	195.621
335.8684	-0.925	7.0	7.0	1168.193
335.8783	-1.418	3.0	3.0	196.557
335.8825	-1.216	6.0	7.0	6932.594
335.8877	-2.109	5.0	4.0	325.748
335.8880	-0.867	8.0	8.0	1457.516
335.8909	-2.156	3.0	4.0	326.030
335.9008	-1.240	4.0	4.0	326.909
335.9023	-2.175	6.0	5.0	488.267
335.9072	-2.220	4.0	5.0	488.704
335.9077	-0.816	9.0	9.0	1777.704
335.9158	-1.117	5.0	5.0	489.460
335.9269	-0.771	10.0	10.0	2128.257
335.9285	-1.024	6.0	6.0	684.226
335.9387	-1.164	7.0	8.0	6933.030
335.9403	-0.949	7.0	7.0	910.637
335.9493	-0.730	11.0	11.0	2509.002
335.9518	-0.885	8.0	8.0	1168.763
335.9637	-0.831	9.0	9.0	1457.811
335.9746	-0.693	12.0	12.0	2919.197
335.9776	-0.783	10.0	10.0	1778.187
335.9928	-0.740	11.0	11.0	2128.525
335.9997	-0.659	13.0	13.0	3358.734
336.0042	-0.820	9.0	9.0	1167.391
336.0046	-0.872	8.0	8.0	909.325
336.0067	-0.774	10.0	10.0	1456.537

Table 10. Molecular data of NH used to synthesise the NH 336 nm band (second part).

λ nm	log gf	J_{low}	J_{up}	E_{low} cm ⁻¹
336.0068	-1.089	8.0	9.0	6931.751
336.0073	-0.932	7.0	7.0	682.958
336.0106	-0.701	12.0	12.0	2509.381
336.0108	-0.732	11.0	11.0	1776.682
336.0165	-1.003	6.0	6.0	488.267
336.0207	-0.694	12.0	12.0	2127.089
336.0275	-0.627	14.0	14.0	3826.364
336.0300	-2.159	5.0	6.0	489.460
336.0308	-0.666	13.0	13.0	2919.347
336.0318	-1.089	5.0	5.0	325.748
336.0330	-0.660	13.0	13.0	2507.714
336.0364	-1.388	3.0	4.0	3219.414
336.0449	-2.082	4.0	5.0	326.909
336.0483	-0.628	14.0	14.0	2917.983
336.0542	-0.633	14.0	14.0	3358.909
336.0585	-1.201	4.0	4.0	195.513
336.0617	-0.597	15.0	15.0	4322.481
336.0678	-0.598	15.0	15.0	3357.108
336.0703	-1.992	3.0	4.0	196.557
336.0795	-0.603	15.0	15.0	3826.473
336.0901	-0.570	16.0	16.0	3825.097
336.0986	-0.570	16.0	16.0	4845.503
336.1004	-1.361	3.0	3.0	97.718
336.1098	-0.574	16.0	16.0	4322.581
336.1112	-1.885	2.0	3.0	98.676
336.1179	-0.544	17.0	17.0	4320.719
336.1420	-0.544	17.0	17.0	5395.737
336.1426	-0.548	17.0	17.0	4845.563
336.1445	-1.846	2.0	2.0	3156.788
336.1487	-0.520	18.0	18.0	4843.941
336.1497	-1.283	5.0	6.0	6724.005
336.1728	-1.642	2.0	2.0	32.506
336.1825	-1.760	1.0	2.0	33.359
336.1833	-0.497	19.0	19.0	5393.767
336.1837	-0.523	18.0	18.0	5395.779
336.1886	-0.519	18.0	18.0	5971.663
336.2137	-1.224	6.0	7.0	6724.585
336.2275	-0.474	20.0	20.0	5969.806
336.2282	-0.500	19.0	19.0	5971.682
336.2381	-0.496	19.0	19.0	6573.346